NASA TECHNICAL REPORT

NASA TR R-256

NASA TR R-256

FLUTTER ANALYSIS OF FLAT RECTANGULAR PANELS BASED ON THREE-DIMENSIONAL SUPERSONIC UNSTEADY POTENTIAL FLOW

by Herbert J. Cunningham

Langley Research Center

Langley Station, Hampton, Va.

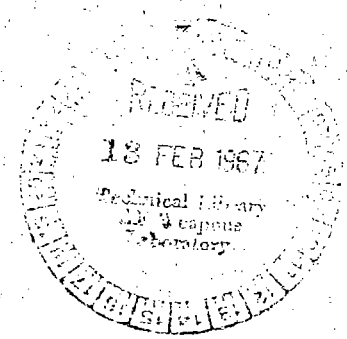

NATIONAL AERONAUTICS AND SPACE ADMINISTRATION • WASHINGTON, D. C. • FEBRUARY 1967

NASA TR R-256

FLUTTER ANALYSIS OF FLAT RECTANGULAR PANELS BASED ON THREE-DIMENSIONAL SUPERSONIC UNSTEADY POTENTIAL FLOW

By Herbert J. Cunningham

Langley Research Center
Langley Station, Hampton, Va.

NATIONAL AERONAUTICS AND SPACE ADMINISTRATION

For sale by the Clearinghouse for Federal Scientific and Technical Information
Springfield, Virginia 22151 – Price $2.00

FLUTTER ANALYSIS OF FLAT RECTANGULAR PANELS BASED ON THREE-DIMENSIONAL SUPERSONIC UNSTEADY POTENTIAL FLOW

By Herbert J. Cunningham
Langley Research Center

SUMMARY

A systematic analytical procedure has been developed for computing flutter characteristics of rectangular panels with stream-alined side edges, based on air forces from three-dimensional linearized supersonic unsteady potential flow. The procedure has particular usefulness in the low supersonic speed range where static and quasi-static aerodynamic approximations are considered to be least valid and can provide bases of comparison for some of the simpler types of analysis. The panel is considered to be finely divided into many boxes, and the aerodynamic influence coefficients between all pairs of boxes are obtained by numerical integration. The flutter analysis is a modal type, which readily coordinates with the aerodynamic box method, and can be used for calculating the flutter stability of any flat or nearly flat panel, whether of isotropic or anisotropic stiffness, and of buckled panels for which the flutter is a small-amplitude, simple harmonic, superimposed motion to which linear theory is applicable. A number of results are presented for flat unstressed, isotropic panels with simply supported edges and with clamped edges. For clamped-edge aluminum panels with a length-width ratio of 2 at sea level, the panel flutter parameters are tabulated for eight Mach numbers ranging from 1.02 to 2.0. For Mach 1.3, flutter boundaries are plotted for length-width ratios from 0 to 10 for simply supported edges and from 0 to 4 for clamped edges so that design values can be read for a wide range of panel materials and air densities. Appendix A delineates the way in which the natural mode characteristics were developed for calculating the presented flutter results without the need for double-precision arithmetic. Appendix B provides formulas for conversion among a number of types of flutter solution parameters in current use. Appendix C describes a way to economize computer time for the large matrix multiplications required.

INTRODUCTION

A description of an analysis of the flutter of flat rectangular unyawed panels on the basis of unsteady potential flow and some results from that analysis were presented in

reference 1. Since its publication, considerably more information and results have been obtained. The purpose of this report is to present the overall results. The description of the analysis is sufficiently complete to enable the analyst to understand it without referring to reference 1.

In the lower supersonic Mach number range, below a Mach number of about $\sqrt{2}$, simple approximations for the aerodynamic forces, such as Ackeret theory or piston theory, do not give satisfactory results, at least for panel length-width ratios less than about 1.0. For length-width ratios greater than 1.0, there is now some evidence that Ackeret and piston theory can give good estimates of the panel thickness required to prevent flutter, and this evidence is discussed in the present report.

The central feature of this analysis is the way in which the aerodynamic forces are determined. In what has come to be known in the literature as a "box method," the required double surface integration is carried out by considering the panel to be finely divided into a large number of equal-size rectangular elements or "boxes." The aerodynamic influence coefficient relating the velocity potential of each box to the motion of each other box is calculated by numerical integration and used in a modal-type flutter stability solution. Mode-shape properties from either calculation or experimental measurement can be applied in the flutter solution.

A variety of flutter results are presented and discussed for flat unstressed panels with isotropic stiffness. Calculated mode shapes and frequencies were used. Although the results presented are limited to simple panels, this type of modal analysis with a box method is broadly applicable to flat or nearly flat panels, whether unstressed or stressed (as by thermal expansion), and whether of isotropic or anisotropic stiffness. It would also seem to be applicable to buckled panels for which the flutter is a small-amplitude, simple harmonic, superimposed motion to which linear theory would apply.

A brief discussion is given of recently published findings that the stiffness coupling effects between assumed beam natural modes, when they are applied to the flutter analysis of clamped-edge plates, are not uniformly negligible and can become significantly large as length-width ratio increases.

Appendix A presents the expressions for the panel vibration mode shapes and frequencies used in the flutter analysis in such forms that only single-precision arithmetic is necessary for all modes used. Appendix B gives the relations among some panel flutter parameters that are used in the literature. Appendix C describes a way to economize computer time for the large matrix multiplication in computing the velocity potentials.

SYMBOLS

a_s speed of sound

A_φ aerodynamic influence coefficient giving the velocity potential at a box induced due to unit downwash on another box (eqs. (13) and (18))

B_S, B_{XS} number of boxes in stream and cross-stream directions, respectively

D flexural stiffness of an isotropic panel

E Young's modulus of elasticity

g, g_i coefficients of mechanical hysteretic structural damping

$g_I = g_i + g$

h_i, h_j amplitude of natural mode-shape deflection for modes i and j

$H_j(x,y,\tau)$ distribution of time-varying panel deflection for mode j (eq. (2)), positive downward

$i = \sqrt{-1}$

I_{G1}, I_{G2}, I_{G3} integrals in A_φ (eqs. (19) to (21))

k_ϵ reduced frequency with reference length ϵ, $\frac{\omega\epsilon}{V}$

k_l reduced frequency with reference length l, $\frac{\omega l}{V}$

K_p, K_q roots of characteristic equations (eqs. (A3), (A7), and (A13))

$K^*_{p,q}$ nondimensional eigenvalue quantity for natural vibration modes (eqs. (A4), (A12), (A17), and (A18))

l length of panel in stream direction

m_A mass of panel per unit of surface area

M Mach number, $\frac{V}{a_s}$

M_i generalized mass for mode i

$M_i^* = \frac{M_i}{\ell w m_A}$ (applicable for uniform panel only)

p,q number of half-waves in panel vibration mode in stream and cross-stream directions, respectively

Δp perturbation lifting pressure, positive downward

Δp_j perturbation pressure due to mode j (eqs. (5) and (7)), positive sense same as that for H_j

q free-stream dynamic pressure, $\frac{\rho V^2}{2}$

$\bar{q}_i(\tau),\bar{q}_j(\tau)$ time-varying generalized coordinate of motion for modes i and j, respectively

q_j complex amplitude of $\bar{q}_j(\tau)$ (eq. (2)); also the eigenvector for mode j from a flutter solution

Q_{ij} generalized aerodynamic force from pressure due to mode j and modal deflection of mode i (eqs. (8) to (10))

Q_{ij}^* nondimensional computational quantity contained in Q_{ij} (eq. (28))

S panel area

t thickness of panel

u,v transformed panel coordinates and variables of integration in x- and y-directions, respectively, based on $\epsilon/2$ as a reference length, (eq. (15))

u_1,u_2,v_1,v_2 lower and upper limits of integration with respect to u and to v (eq. (16) and table I)

V speed of undisturbed airstream

w width of panel in cross-stream direction

w_j downwash velocity at panel surface for mode j, positive downward

x,y panel coordinates in stream and cross-stream directions, respectively (see fig. 1)

x_ϵ, y_ϵ panel coordinates based on ϵ as a reference length, $x_\epsilon = \frac{x}{\epsilon}$, $y_\epsilon = \frac{y}{\epsilon}$

x_m, y_n values of x_ϵ and y_ϵ at center of box m,n (see fig. 1)

$\bar{x}, \bar{y}$ panel coordinates based on reference lengths l and w, respectively

X_j, Y_j x- and y-variation, respectively, of H_j (eq. (A1))

z panel deflection, positive downward, $Z(x,y)e^{i\omega\tau}$

$\alpha = \rho \frac{l}{B_s}\left(\frac{w}{B_{xs}}\right)^2$

$\alpha^* = \frac{w}{l} B_s B_{xs}^2$

$\alpha_{p,x}, \alpha_{q,y}$ eigenvalue quantities for x- and y-variations, respectively, of assumed beam modes (eqs. (A5) and (A10))

$\beta = \sqrt{M^2 - 1}$

ϵ width of box, $\frac{w}{B_{xs}}$

ϵ_p, ϵ_q small difference quantities (see eqs. (A8) and (A14))

η dummy variable of integration for y_ϵ

λ dynamic pressure parameter, $\frac{2ql^3}{\beta D}$

μ ratio of panel mass density to air mass density, $\frac{m_A}{\rho l}$

ξ dummy variable of integration for x_ϵ

ρ density of undisturbed airstream

σ length-width ratio of box, $\frac{l B_{xs}}{w B_s}$

τ time

φ_j velocity potential at center of box m,n for mode j, $\varphi_j(m,n)$

$\varphi_j^*(m,n)$ nondimensional part of $\varphi_j(m,n)$ (eqs. (26) and (27))

$\overline{\varphi}$ velocity potential at center of box m,n due to unit downwash over box μ,ν

ω frequency of flutter motion

ω_j, ω_B natural frequencies of panel mode j and of a chosen base or reference mode, respectively

$\Omega = \left(\frac{\omega_B}{\omega}\right)^2 (1 + ig)$ flutter eigenvalue parameter

$\overline{\Omega} = \frac{M^2 k_\epsilon}{\beta^2}$

[ ], [ ], { } row, rectangular, and column matrices, respectively

Subscripts and index numbers:

B base or reference value

i,j mode numbers

m,n streamwise and cross-stream numbered location of a receiving box

p,q number of half-waves in stream and cross-stream directions, for a panel vibration mode

r,s relative numbered locations of sending and receiving boxes, (eq. (12))

te value at trailing edge of panel

x,y x- and y-directions or variations

μ,ν streamwise and cross-stream numbered location of a sending box

ANALYSIS

Statement of Problem

The panel to be analyzed and the coordinate system used are shown in figure 1. The panel is a single rectangular panel of length l, width w, and the side edges are alined with the remote wind direction. It is a flexible part of an otherwise inflexible surface that extends at least far enough to the sides to prevent the upper and lower surfaces of the panel inducing any aerodynamic effects upon each other. Supersonic flow over the upper surface only is considered. The analysis is made on the basis of linear relations between small deflections and applied loads.

Since the primary contribution of the present report is the procedure for obtaining the generalized aerodynamic forces for use in a flutter analysis, the governing differential equation of motion is written, for simplicity of presentation, for a uniform isotropic plate with no in-plane loading

$$D\left(\frac{\partial^4 z}{\partial x^4} + 2\frac{\partial^4 z}{\partial x^2 \partial y^2} + \frac{\partial^4 z}{\partial y^4}\right) + m_A \frac{\partial^2 z}{\partial \tau^2} - \Delta p(x,y,\tau) = 0 \qquad (1)$$

where z is the deflection (positive downward) of the panel, D is the panel flexural stiffness, m_A is the mass per unit area of the panel, and Δp is the net perturbation pressure (positive downward) arising from the deflection and motion of the panel. Equation (1) does not have an explicit term for damping in the structure but any damping consistent with a linear treatment can be introduced.

For the type of panel deflections and aerodynamic forces considered, it has not been found feasible to make a direct solution to the equation of motion. Therefore, the often-used procedure is followed, of considering the panel deflection to be sufficiently well approximated by a finite series, that is, a linear combination of prechosen deflection modes. For simple harmonic motion $z(x,y,\tau) = Z(x,y)e^{i\omega\tau}$, where ω is the circular frequency of

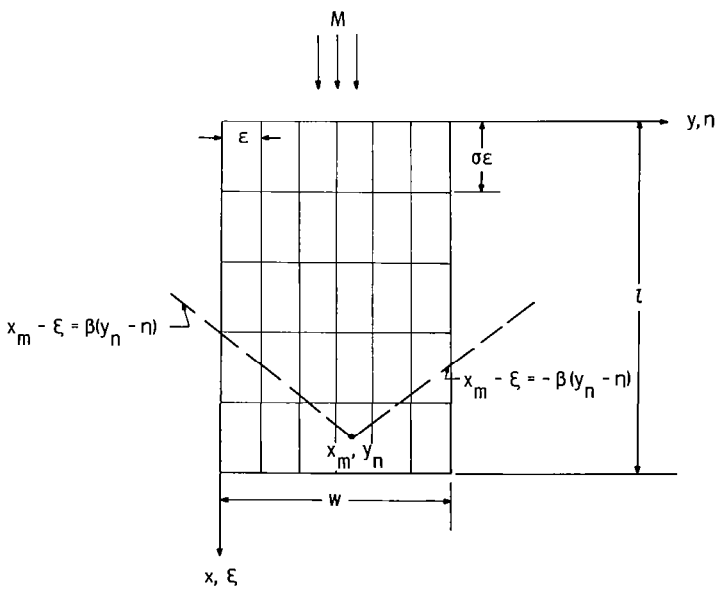

Figure 1.- Plan view of panel divided into boxes with coordinate system, dimensions, and a forward facing Mach cone with apex at box center x_m, y_n.

vibration and where $Z(x,y)$ can be a complex function to account for phase differences of motion over the panel.

This procedure leads to

$$\left.\begin{aligned} z(x,y,\tau) &\approx \sum_j H_j(x,y,\tau) \\ H_j(x,y,\tau) &= \bar{q}_j(\tau)h_j(x,y) = q_j e^{i\omega\tau}h_j(x,y) \end{aligned}\right\} \tag{2}$$

and q_j is the complex amplitude of the generalized coordinate of motion. If the deflection mode shapes h_j are known that satisfy exactly both the geometric boundary conditions and the differential equation that corresponds to equation (1) without the aerodynamic term, then (the time variation $e^{i\omega\tau}$ being set aside)

$$D\left(\frac{\partial^4 h_j}{\partial x^4} + 2\frac{\partial^4 h_j}{\partial x^2 \partial y^2} + \frac{\partial^4 h_j}{\partial y^4}\right) = -m_A \frac{\partial^2 (H_j/q_j)}{\partial \tau^2} e^{-i\omega\tau} = m_A \omega_j{}^2 h_j \tag{3}$$

where on the right-hand side ω takes on its eigenvalue ω_j, the normal mode frequency associated with h_j. The consequences of using shapes h_j that fail to satisfy exactly the differential equations are examined and discussed later for clamped-edge panels. Substitution of equation (2) into equation (1) and application of equation (3) produce the result

$$\sum_j \bar{q}_j h_j m_A \omega_j{}^2 - \sum_j \bar{q}_j h_j m_A \omega^2 - \Delta p(x,y,\tau) = 0 \tag{4}$$

in which the frequency ω and the combination of $\bar{q}_j$ are unknown, and the perturbation pressure Δp still has to be determined.

Consistent with the use of a series representation of the panel deflection, the pressure distribution Δp is also used as a series, one term being associated with each deflection mode,

$$\Delta p \approx \sum_j \Delta p_j = \sum_j \bar{q}_j \overline{\Delta p}_j \tag{5}$$

where Δp_j is separated into the time containing $\bar{q}_j$ and the time invariant $\overline{\Delta p}_j$.

The Galerkin method is chosen to form the flutter stability equations. Briefly described, the terms of equation (4) are multiplied by a mode shape $h_i(x,y)$ and the products are integrated over the surface area of the panel. When the modal index number i is made successively 1, 2, 3, . . . for all the modes h_i employed, the result is

a system of equations that requires an equilibrium of work or energy for a condition of minimum total (kinetic plus elastic potential) energy of the panel. For modes h_j that satisfy equation (3) and are orthogonal, each of the equations is of the relatively simple form

$$\sum_j \bar{q}_j\left(\omega_j{}^2 - \omega^2\right)\iint_S m_A h_j h_i \, dx\, dy - \sum_j \bar{q}_j \iint_S \left(\overline{\Delta p}_j\right) h_i \, dx\, dy = 0 \tag{6}$$

and the last term $\bar{q}_j \iint_S \overline{\Delta p}_j h_i \, dx\, dy \equiv Q_{ij}$ is the generalized aerodynamic force term.

In order to obtain the pressures $\overline{\Delta p}_j = \bar{q}_j \, \overline{\Delta p}_j$, the choice is made to work with the velocity potential φ_j and make use of the relation (compare eq. (3) of ref. 2, for example)

$$\Delta p_j = -\rho \frac{d\varphi_j}{d\tau} = -\rho\left(V \frac{\partial \varphi_j}{\partial(l\bar{x})} + \frac{\partial \varphi_j}{\partial \tau}\right) = -\frac{\rho V}{l}\left(\frac{\partial \varphi_j}{\partial \bar{x}} + i \frac{\omega l}{V} \varphi_j\right) \tag{7}$$

where ρ and V are the mass density and velocity of the undisturbed airstream. Each of the generalized aerodynamic force terms Q_{ij} needed in the dynamic equilibrium flutter equations is the integral over the panel surface of work that would be done on modal displacement i with unit amplitude due to a deflection in mode j with amplitude $\bar{q}_j$; that is,

$$Q_{ij} = -\frac{\rho V}{l} \iint_S h_i\left(\frac{\partial \varphi_j}{\partial \bar{x}} + i \frac{\omega l}{V} \varphi_j\right) d(l\bar{x}) d(w\bar{y}) \tag{8}$$

where here and in the following development the subscript index for mode i is not to be confused with the unit of imaginaries $i \equiv \sqrt{-1}$. The coordinate $\bar{y}$ ranges from 0 at the left edge to 1.0 at the right edge. If the term $h_i\left(\partial \varphi_j / \partial \bar{x}\right)$ is integrated by parts, the result is

$$Q_{ij} = -\frac{\rho V}{l} \int_{\bar{y}=0}^{1} \left[h_i\left(x_{te}, y\right) \varphi_j\left(x_{te}, y\right) - \int_{\bar{x}=0}^{1} \varphi_j \left(\frac{\partial h_i}{\partial \bar{x}} - i \frac{\omega l}{V} h_i\right) d(l\bar{x}) \right] d(w\bar{y}) \tag{9}$$

For elastically supported or free trailing edges, the trailing-edge deflection $h_i\left(x_{te}, y\right)$ could be significant, but for the usual condition of a restrained trailing edge, it is zero, and Q_{ij} is determined from the second term only as

$$Q_{ij} = \frac{\rho V}{l} \iint_S \varphi_j \left(\frac{\partial h_i}{\partial \bar{x}} - i \frac{\omega l}{V} h_i\right) d(l\bar{x}) d(w\bar{y}) \tag{10}$$

Note that the quantity within the parentheses is the complex conjugate of the downwash ratio.

In most of the foregoing equations, the harmonic time variation $e^{i\omega\tau}$ is retained, but except at points where the time derivative $\partial/\partial\tau$ is indicated, the quantities φ_j and Q_{ij} can be considered alternatively as their complex amplitudes only.

In the rest of this section the procedures for computing (1) the aerodynamic influence coefficients relating downwash and velocity potential, (2) the velocity potentials, and (3) the generalized aerodynamic forces are described. The procedure used for obtaining solutions to the system of flutter equilibrium equations is also described.

Aerodynamic Influence Coefficient

The panel is considered as divided into a gridwork of equal-size rectangular "boxes." The number of boxes in the stream and cross-stream directions are B_S and B_{XS}, respectively. For reference in the computation procedure, the boxes are numbered in sequence beginning at the box nearest the origin of coordinates; in the stream direction the index $m = 0, 1, 2, \ldots B_S - 1$, and in the cross-stream direction $n = 0, 1, 2, \ldots B_{XS} - 1$. A second set of box index numbers is needed, and these numbers, designated by μ and ν, take on values $\mu = 0, 1, 2, \ldots B_S - 1$ and $\nu = 0, 1, 2, \ldots B_{XS} - 1$. Thus, reference can be made to the aerodynamic influence upon any receiving box m,n due to any sending box μ,ν.

The gridwork of boxes is assumed to be sufficiently fine so that the downwash over any sending box can be taken as uniformly distributed at any instant, and that the resulting pressure perturbation at the center of each receiving box is a sufficiently accurate average of the pressure distribution over that box.

For convenience in the computational procedure, a reference length has been chosen as $\epsilon = \frac{w}{B_{XS}}$, the width of a box. The velocity potential at the center of a receiving box m,n due to a uniformly distributed but otherwise unspecified downwash $w(\mu,\nu)$ over the sending box μ,ν can be expressed for a simple harmonic time variation (compare eq. (34) of ref. 2) as

$$\overline{\varphi}(m,n) = \epsilon w(\mu,\nu)\, A_{\varphi}(r,s) \tag{11}$$

where the relative locations fore and aft, and sidewise, respectively, of the two boxes are indicated by

$$\left.\begin{aligned} r &= m - \mu \\ s &= n - \nu \end{aligned}\right\} \tag{12}$$

and from equation (34) of reference 2

$$A_\varphi(r,s) = \frac{1}{\pi} \iint_{S_{\mu,\nu}} \frac{e^{-i\overline{\Omega}(x_m-\xi)} \cos\left\{\frac{\overline{\Omega}}{M}\left[(x_m-\xi)^2 - \beta^2(y_n-\eta)^2\right]^{1/2}\right\}}{\left[(x_m-\xi)^2 - \beta^2(y_n-\eta)^2\right]^{1/2}} d\xi\, d\eta \tag{13}$$

in which the area of integration $S_{\mu,\nu}$ is any part of the sending box μ,ν that lies forward of the forward-facing Mach cone with apex at x_m,y_n. (See fig. 1.) Note that the integrand is singular along the Mach cone because of the denominator. All boxes and parts of boxes lying aft of that Mach cone have a zero contribution to $A_\varphi(r,s)$. For box m,n the coordinates x_m and y_n and their respective dummy variables of integration ξ and η are based on the reference length ϵ; that is, $x_m = \frac{x}{\epsilon}$ and $y_n = \frac{y}{\epsilon}$. The frequency Mach number parameter $\overline{\Omega}$ is

$$\overline{\Omega} \equiv \frac{M^2 k_\epsilon}{\beta^2} \tag{14}$$

where the reduced frequency $k_\epsilon \equiv \frac{\omega\epsilon}{V}$ contains the chosen reference length ϵ.

As in reference 2, a transformation of variables is made as follows:

$$\left.\begin{aligned} x_m - \xi &= \frac{\beta u}{2} \\ y_n - \eta &= \frac{v}{2} \end{aligned}\right\} \tag{15}$$

With transformation equations (15), equation (13) becomes

$$A_\varphi(r,s) = \frac{1}{2\pi} \int_{u_1}^{u_2} e^{-i(\beta\overline{\Omega}/2)u} du \int_{v_1}^{v_2} \frac{\cos\left[\frac{\beta\overline{\Omega}}{2M}(u^2 - v^2)^{1/2}\right]}{(u^2 - v^2)^{1/2}} dv \tag{16}$$

where the upper and lower limits of the surface integrals, indicated by v_1, v_2, u_1, and u_2, are established for any given box by its edges except where the forward Mach cone with apex at x_m,y_n passes through the box.

The integral of equation (16) is to be evaluated numerically. The integrand contains a singularity of order -1/2, at $u = \pm v$, that is, along the Mach lines from x_m,y_n. In order to minimize the potential inaccuracies in integrating by numerical quadrature in the vicinity of that singularity, the numerator of the integrand is replaced by the identity

$$\cos\left[\frac{\beta\bar{\Omega}}{2M}\left(u^2 - v^2\right)^{1/2}\right] \equiv \left\{\cos\left[\frac{\beta\bar{\Omega}}{2M}\left(u^2 - v^2\right)^{1/2}\right] - 1\right\} + 1 \tag{17}$$

Substituting equation (17) into equation (16) and carrying out formally part of the v integration gives

$$A_\varphi(r,s) = \frac{1}{2\pi}\int_{u_1}^{u_2} e^{-i(\beta\bar{\Omega}/2)u}\left(\cos^{-1}\frac{v_1}{u} - \cos^{-1}\frac{v_2}{u} + \int_{v_1}^{v_2}\frac{\cos\left[\frac{\beta\bar{\Omega}}{2M}\left(u^2 - v^2\right)^{1/2}\right] - 1}{\left(u^2 - v^2\right)^{1/2}}\,dv\right)du \tag{18}$$

where the integrand of the remaining v integral is zero at $u = \pm v$ and numerical integration with good accuracy is possible. All possible forms of the limits u_1, u_2, v_1, and v_2 lead to only three forms of equation (18) that are explained with the aid of table I. The first form is for the condition $v_2 = -v_1 = u$ that can occur only for $\nu = n$ (that is, $s = 0$), and then only for any portion of a sending box μ,ν cut by both sides of the Mach cone. For this condition

$$I_{G1} = \frac{1}{2}\int_{u_1}^{u_2} e^{-i(\beta\bar{\Omega}/2)u} J_0\left(\frac{\beta\bar{\Omega}}{2M}u\right)du \tag{19}$$

where J_0 is the Bessel function of the first kind of order zero. The second form of equation (18) occurs for portions of a box cut by one side of the Mach cone ($s \neq 0$), so that the limit $v_2 = u$ and $v_1 = 2s - 1 \geq 1$. Since $v_2 = u$, $\cos^{-1}\frac{v_2}{u} = 0$ and

$$I_{G2} = \frac{1}{2\pi}\int_{u_1}^{u_2} e^{-i(\beta\bar{\Omega}/2)u}\left(\cos^{-1}\frac{v_1}{u} + \int_{v_1}^{u}\frac{\cos\left[\frac{\beta\bar{\Omega}}{2M}\left(u^2 - v^2\right)^{1/2}\right] - 1}{\left(u^2 - v^2\right)^{1/2}}\,dv\right)du \tag{20}$$

The third form, which occurs for boxes that are completely ahead of the Mach cone and also for portions of boxes ahead of the point where the Mach cone passes out through the side of the box, is

$$I_{G3} = \frac{1}{2\pi}\int_{u_1}^{u_2} e^{-i(\beta\bar{\Omega}/2)u}\left(\cos^{-1}\frac{v_1}{u} - \cos^{-1}\frac{v_2}{u} + \int_{v_1}^{v_2}\frac{\cos\left[\frac{\beta\bar{\Omega}}{2M}\left(u^2 - v^2\right)^{1/2}\right] - 1}{\left(u^2 - v^2\right)^{1/2}}\,dv\right)du \tag{21}$$

The complete $A_\varphi(r,s)$ for any one box μ,ν consists entirely of I_{G1}, I_{G2}, or I_{G3}, or a combination of I_{G1} and I_{G3} or of I_{G2} and I_{G3}.

Table I.- Types of integrals and limits of integration for computing $A_{\varphi}(r,s)$ for all possible relative locations of box μ,ν and the Mach cone from box m,n.

		Limits of integration			
		v_1	v_2	u_1	u_2
s = 0	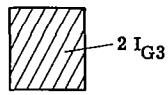 $2\,I_{G3}$	0	1	$(2r - 1)\,\sigma/\beta$	$(2r + 1)\,\sigma/\beta$
	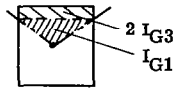 $2\,I_{G3}$ I_{G1}	0 -----	1 -----	1 0	$(2r + 1)\,\sigma/\beta$ 1
	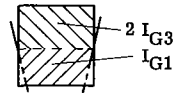 $2\,I_{G3}$ I_{G1}	0 -----	1 -----	1 $(2r - 1)\,\sigma/\beta$	$(2r + 1)\,\sigma/\beta$ 1
	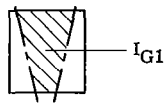 I_{G1}	-----	-----	$(2r - 1)\,\sigma/\beta$	$(2r + 1)\,\sigma/\beta$
	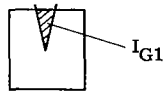 I_{G1}	-----	-----	0	$(2r + 1)\,\sigma/\beta$
s > 0	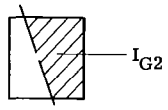 I_{G2}	$2s - 1$	u	$(2r - 1)\,\sigma/\beta$	$(2r + 1)\,\sigma/\beta$
	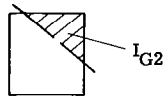 I_{G2}	$2s - 1$	u	$2s - 1$	$(2r + 1)\,\sigma/\beta$
	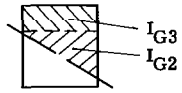 I_{G3} I_{G2}	$2s - 1$ $2s - 1$	$2s + 1$ u	$2s + 1$ $2s - 1$	$(2r + 1)\,\sigma/\beta$ $2s + 1$
	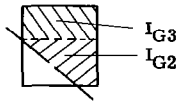 I_{G3} I_{G2}	$2s - 1$ $2s - 1$	$2s + 1$ u	$2s + 1$ $(2r - 1)\,\sigma/\beta$	$(2r + 1)\,\sigma/\beta$ $2s + 1$
	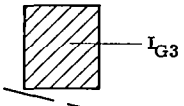 I_{G3}	$2s - 1$	$2s + 1$	$(2r - 1)\,\sigma/\beta$	$(2r + 1)\,\sigma/\beta$
	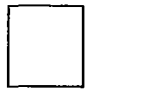	$A_{\varphi}(r,s) = 0$			

Table I covers all possible relative locations of a sending box and the Mach cone from a receiving box. The applicable integral, I_{G1}, I_{G2}, or I_{G3}, for a box or box segment and the limits of integration v_1, v_2, u_1, and u_2 are listed. The limits tabulated are consistent with the reference length ϵ chosen for equation (11) and with the transformation of equation (15). The double quantity $2I_{G3}$ appears in table I where advantage was taken of symmetry about $v_1 = 0$. The quantity $\sigma = \frac{\ell B_{xs}}{wB_s}$ is the length-width ratio of a box.

For the unyawed panel with the assumptions that have been made, the aerodynamic influence coefficients have right-left symmetry about $s = 0$; that is,

$$A_\varphi(r,s) = A_\varphi(r,-s) \tag{22}$$

Thus, all values of $A_\varphi(r,s)$ that are needed for any box are obtained by considering either one of the rear corner boxes as the receiving box. Both the u and v integrals are carried out in the computing program according to Gaussian numerical quadrature (described in numerous texts, for example, ref. 3) by an available subroutine. For sending boxes near the Mach cone from x_m,y_n, a five-point integrating rule was found to be accurate. For sending boxes remote from the Mach cone, a three-point rule was found to be accurate and provided a consequent economy of machine time.

Velocity Potentials

Once all possible values of $A_\varphi(r,s)$ are computed, the total $\varphi_j(m,n)$ at the center of any box m,n for any downwash mode j is a weighted sum of the $\overline{\varphi}(m,n)$ of equation (11) particularized to mode j; that is,

$$\varphi_j(m,n) = V\epsilon \sum_{\mu} \sum_{\nu} \frac{w_j(\mu,\nu)}{V} A_\varphi(r,s) \tag{23}$$

or, in matrix form

$$\varphi_j(m,n) = V\epsilon \left[\frac{w_j(\mu,\nu)}{V}\right] \left\{A_\varphi(r,s)\right\} \tag{24}$$

The downwash ratios $\frac{w_j(\mu,\nu)}{V}$ are the total time derivatives of H_j

$$\frac{w_j}{V} = \frac{1}{V}\frac{dH_j}{d\tau} = \frac{\partial H_j}{\partial(\ell \bar{x})} + \frac{1}{V}\frac{\partial H_j}{\partial \tau} = \frac{\bar{q}_j}{\ell}\left(\frac{\partial h_j}{\partial \bar{x}} + i\,\frac{\omega \ell}{V} h_j\right) \tag{25}$$

Of course, a complete array of $\varphi_j(m,n)$ is required to cover all m,n. With a dimensional constant separated, the complete array is

$$\left\{\varphi_j(m,n)\right\} = V\epsilon \frac{\bar{q}_j}{l}\left\{\varphi_j{}^*(m,n)\right\} \tag{26}$$

where the nondimensional elements $\varphi_j{}^*(m,n)$ are

$$\left\{\varphi_j{}^*(m,n)\right\} = \left[\frac{\partial h_j}{\partial \bar{x}} + i\frac{\omega l}{V} h_j\right]\left\{A_\varphi(r,s)\right\} \tag{27}$$

in which h_j is $h_j(x_\mu, y_\nu)$.

The practicality of this box method is largely dependent on the machine time consumed in the matrix multiplication of equation (27) for multiple modes j. An economical way to obtain the matrix of $\varphi_j{}^*$ is described in appendix C.

Generalized Aerodynamic Forces

Equation (10) represents a generalized aerodynamic force term as a surface integral. With use of the box method, the terms are evaluated by a matrix multiplication. With a dimensional constant separated

$$Q_{ij} = \rho V^2 \frac{w^2}{B_s B_{xs}{}^2} \frac{\bar{q}_j}{l} Q^*_{ij} \tag{28}$$

the nondimensional part is

$$Q^*_{ij} = \left[\frac{\partial h_i}{\partial \bar{x}} - i\frac{\omega l}{V} h_i\right]\left\{\varphi_j{}^*\right\} \tag{29}$$

To conserve machine core storage, the real and imaginary part of the downwash from equation (27) can be used in its complex conjugate in equation (29).

The complete matrix of elements Q^*_{ij} is obtained by use of successive rows of the downwash conjugate with one row for each mode i and successive columns of $\varphi_j{}^*$ with one column for each mode j.

Solution of the Flutter Determinant

For the numerical solutions presented herein, it has been assumed that the individual modes used in the analysis are orthogonal (that is, with no inertial coupling) and also have no significant stiffness coupling between modes. Recent findings, that for clamped-edge panels stiffness coupling can be significant, are discussed in the section "Results and Discussion." Further, structural hysteretic damping that is characterized by a coefficient for each vibration mode is assumed. With these assumptions, the system of

equations that express the dynamic equilibrium of motion based on equation (6) are

$$\left[\omega^2 - \omega_i^2\left(1 + ig_I\right)\right]M_i\bar{q}_i + \sum_j Q_{ij} = 0 \qquad (i = 1, 2, \ldots) \quad (30)$$

where ω_i is the natural frequency of mode i and M_i is the generalized mass of mode i

$$M_i = \ell w \int_0^1 \int_0^1 m_A(x,y)\left[\bar{h}_i(x,y)\right]^2 d\bar{x}\, d\bar{y} \qquad (31)$$

and where m_A represents the distributed panel mass per unit area. In equation (30) the quantity $g_I(<<1)$ is intended to be interpreted as the modal damping coefficient for structural hysteretic damping and is made up of two parts

$$g_I = g_i + g$$

where g_i can be the assigned or measured values for each mode i of the structure and g is a modal-independent mathematical convenience to aid in determining eigensolutions. Let use be made of the asymptotic expression that is applicable for $g << 1$ and $g_i << 1$ and exact for either $g_i = 0$ or $g = 0$

$$1 + ig_i + ig \sim \left(1 + ig_i\right)(1 + ig) \qquad (32)$$

If equation (30) is multiplied by $\dfrac{(\omega_B/\omega_i\omega)^2}{M_i\left(1 + ig_i\right)}$, a form convenient for eigensolution results

$$\left[-\Omega + \left(\frac{\omega_B}{\omega_i}\right)^2 \frac{1}{1 + ig_i}\right]\bar{q}_i + \left(\frac{\omega_B}{\omega_i}\right)^2 \frac{\alpha}{\left(1 + ig_i\right)k_\ell^2 M_i} \sum_j \bar{q}_j Q_{ij}^* = 0 \qquad (i = 1, 2, \ldots) \qquad (33)$$

where ω_B is any chosen base or reference frequency,

$$\Omega \equiv \left(\frac{\omega_B}{\omega}\right)^2 (1 + ig)$$

$$\alpha \equiv \rho \frac{\ell}{B_S}\left(\frac{w}{B_{xs}}\right)^2$$

and $k_\ell = \dfrac{\omega\ell}{V}$ is the reduced frequency based on the reference length ℓ.

In the set of equations indicated by equation (33), the analyst can readily apply values of g_i that are not necessarily the same for the various modes i. Of course, for the situation where the g_i for all modes are equal, $g = g_0$ for illustration, flutter

characteristics that are identical in every respect are computed by either of two processes: (1) Assign $g_i = g_0$ for all modes and determine the crossing point $g = 0$; or (2) Assign $g_i = 0$ for all modes and determine the crossing point $g = g_0$.

For panels with a uniform mass distribution m_A, the quantity α/M_i in equation (33) can be replaced as follows:

$$\frac{\alpha}{M_i} = \frac{\alpha^*}{\mu}\frac{1}{M_i{}^*} \tag{34}$$

where

$$\left.\begin{aligned} \alpha^* &= \frac{w}{\ell B_S B_{xS}{}^2} \\ M_i{}^* &= \int_0^1 \int_0^1 h_i{}^2 d\bar{x}\, d\bar{y} \\ \frac{1}{\mu} &= \frac{\rho \ell}{m_A} \end{aligned}\right\} \tag{35}$$

the ratio of air mass to panel mass being $1/\mu$.

As is commonly the case with the unsteady air forces, the flutter boundary cannot be computed directly, and an indirect method of computing and cross-plotting is necessary. In advance of a flutter solution for any given panel and Mach number, choices are made for B_S, B_{xS} and for the number of modes in the analysis. The downwash quantities $\partial h_i/\partial \bar{x}$ and h_i at the center of each box and the modal frequencies ω_i are computed or obtained from experiment for each mode i and arranged systematically for use in the matrix multiplications. Values of g_i are assigned and the quantities M_i and α (or $M_i{}^*$, $1/\mu$, and α^* for panels with uniform m_A) are computed, except that provision for varying the air density in α (or $1/\mu$) is retained.

After a choice of the reduced frequency k_ℓ based on experience is made, the matrix of values $A_\varphi(r,s)$, the $\varphi_j(m,n)$ at each box center for each mode, and the generalized aerodynamic forces Q_{ij}^* are computed and employed in the flutter determinant, that is, the determinant of the matrix of the coefficients of $\bar{q}_j$ from equation (33). For each of a number of values of the air density, the set of complex eigenvalues Ω, the eigenfrequencies ω, the values of g, and the associated stiffness parameters $\frac{\omega_1 \ell}{V} = \frac{\omega \ell}{V}\frac{\omega_1}{\omega}$ are computed. There is a value of each quantity for each chosen panel mode. The normalized eigenvectors for each eigenfrequency can also be obtained, and can be used to determine the proper plotting of curves through the computed results for a range of k_ℓ or of α^*. By plotting curves of g against $1/\mu$ for a sufficient range of air densities, the existence or nonexistence of an eigenvalue with $g = 0$ for some air density is established for each mode. An associated curve of the stiffness parameter

$\omega_1 l/V$ or $\omega_1 l/a_s$ is plotted against mass ratio – one curve for each eigenvalue. (The use of the speed of sound a_s rather than V permits direct comparison of flutter boundaries for various Mach numbers.)

On a cross plot of $1/\mu$ against stiffness parameter, points can now be placed to represent $g = 0$. Each point is on a separate stability boundary.

By successive choices of k_l based on the results of previous choices, a series of points can be placed on the plot of $1/\mu$, against stiffness parameter, and stability boundaries can be drawn through the points. Four different types of stability boundaries have been found and three types are illustrated in figure 2. For each type, a boundary for $g_i = 0$ and one for $g_i = 0.01$ (as illustrative of some small value) are shown, and the arrows point in the direction of increasing reduced frequency k_l. The boundary of figure 2(a) predicts that if g_i were zero, a fixed panel thickness would be needed as the air density tends toward zero, but if g_i were not zero, panel thickness would go toward zero as air density does.

For the boundary of figure 2(b), the unstable region shrinks with increasing g_i and vanishes for some value that may be extremely small or as large as $g_i = 0.05$ or possibly larger, depending upon the panel and flow parameters. The crossing point of the boundaries for $g_i = 0$ in both figures 2(a) and 2(b) through $\frac{1}{\mu} = 0$ occurs at a value of k_l for which the imaginary part of the $Q_{ii}(k_l)$ passes through zero and the panel motion has a pure single degree of freedom. For the boundary of figure 2(c), the flutter motion is strongly coupled. Small increases of g_i have little or no effect, and this small effect can be either stabilizing or destabilizing, depending on the particular panel and flow parameters. An important point regarding the boundary of figure 2(c), as well as the dashed boundary of figure 2(a), concerns their resemblance to a parabola. For any boundary or portion of a boundary which can be represented by a parabola described by $\frac{1}{\mu} = \left(\frac{\omega_1 l}{a_s}\right)^2$ times a constant, the air density and the panel thickness ratio t/l to prevent flutter are related by the formula $\frac{t}{l(\rho)^{1/2}} = \text{Constant}$. Such a relationship is contained

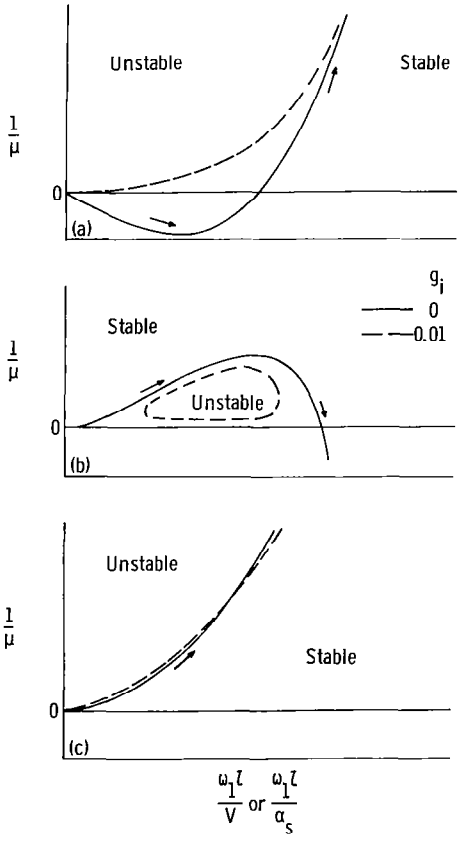

Figure 2.- Three general types of stability boundaries for $g_i = 0$ and for $g_i = 0.01$. Arrows indicate direction of increasing reduced frequency k_l.

in the panel flutter parameter $(E\beta/q)^{1/3}(t/\ell)$, which has been evolved and used by several investigators. The fourth possible type of boundary found from a flutter determinant is one that falls entirely in the negative $1/\mu$ region, the positive $1/\mu$ region being stable with respect to it.

For any given panel and flow parameters, a set of stability boundaries is computed according to the number of modes used in the analysis. The flutter boundary separates the region that is stable with respect to all stability boundaries from the region that is unstable with respect to at least one stability boundary. Care should be taken to establish that the flutter boundary is converged; that is, enough modes have been used in the analysis so that additional modes do not alter the flutter boundary in any important respect. By the Galerkin method alone, it is not usually possible to establish substantial convergence with mathematical rigor. When the incremental effect of additional modes is not only small relative to the magnitude of the calculated quantities, but is also decreasing at a substantial rate as modes are added, near convergence is commonly assumed.

RESULTS AND DISCUSSION

Results that have been calculated by means of the present analysis are presented in a number of figures to scales large enough to permit the reading of values from the flutter boundaries for design purposes. From past work it was established, at least for wide panels (ℓ/w less than about 1.0), that for the low supersonic speed range (M less than about $\sqrt{2}$), approximate aerodynamic forces, such as those of piston theory and static strip theory (the latter is also known as the Ackeret value), do not give valid analytical results. Nevertheless, because of their ease of applications, and because of their application to the higher supersonic speed range, interest in the use of approximate aerodynamic forces has continued. This continuing interest has led to the as-yet-limited finding that for panels that are not wide (ℓ/w greater than about 1.0), approximate aerodynamic forces result in flutter boundaries that agree at least fairly well with the boundaries from the present analysis even in the low supersonic speed range. (See fig. 2 of ref. 4.) On the figures that apply to $\frac{\ell}{w} \geqq 1.0$, therefore, the flutter boundary as obtained from the roots of the closed-form expressions of reference 5 for simply supported panels and of reference 6 for clamped-edge panels (with minor changes for the latter as explained subsequently) is also shown. Reference 5 demonstrates that with static strip-theory aerodynamics on the simply supported panel, the critical flutter mode from the closed-form solution involves a single half-sine wave as its cross-stream variation. The closed-form expressions of reference 6 for the clamped-edge panel were developed on the basis of an assumed single half-wave in the cross-stream direction. Since the natural frequencies for multiple half-wave modes are always higher than those for the single half-wave modes,

and since the aerodynamic cross coupling between single and multiple half-wave modes has been observed to be at least fairly small in comparison with the direct coupling terms, all the results presented in this report are for single half-wave cross-stream modes.

Figures 3 and 5 present the flutter boundaries in plots of the mass ratio $1/\mu$ as the vertical coordinate and the stiffness parameter $\omega_1 l/V$ as the horizontal coordinate. Flutter boundaries are presented for $M = 1.3$ for simply supported panels with length-width ratios of 0, 1/4, 1/2, 1, 2, 4, and 10, and for clamped-edge panels with the same length-width ratios except 10. All the results were obtained or spot-checked with

Quantity	Point A	Point B	Point C
$1/\mu$	0.0240	0.0314	0.0141
g_j	0	0.010	0.010
k_l	0.607	0.50	0.40
$\omega_1 l/V$	0.616	0.5093	0.4035
ω/ω_1	0.985	0.983	0.991
q_1	1.0	1.0	1.0
q_2	$(-0.15 + 0.013i) \times 10^{-1}$	$(-0.27 + 0.017i) \times 10^{-1}$	$(-0.19 + 0.008i) \times 10^{-1}$
q_3	<0.001	$(0.37 - 0.20i) \times 10^{-3}$	$(0.20 - 0.08i) \times 10^{-3}$
q_4	<0.001	$(-0.64 + 0.048i) \times 10^{-3}$	$(-0.45 + 0.022i) \times 10^{-3}$
q_5	<0.0001	$(0.24 - 0.15i) \times 10^{-4}$	$(0.13 - 0.058i) \times 10^{-4}$
q_6	<0.0001	$(-0.80 + 0.062i) \times 10^{-4}$	$(-0.57 + 0.028i) \times 10^{-4}$

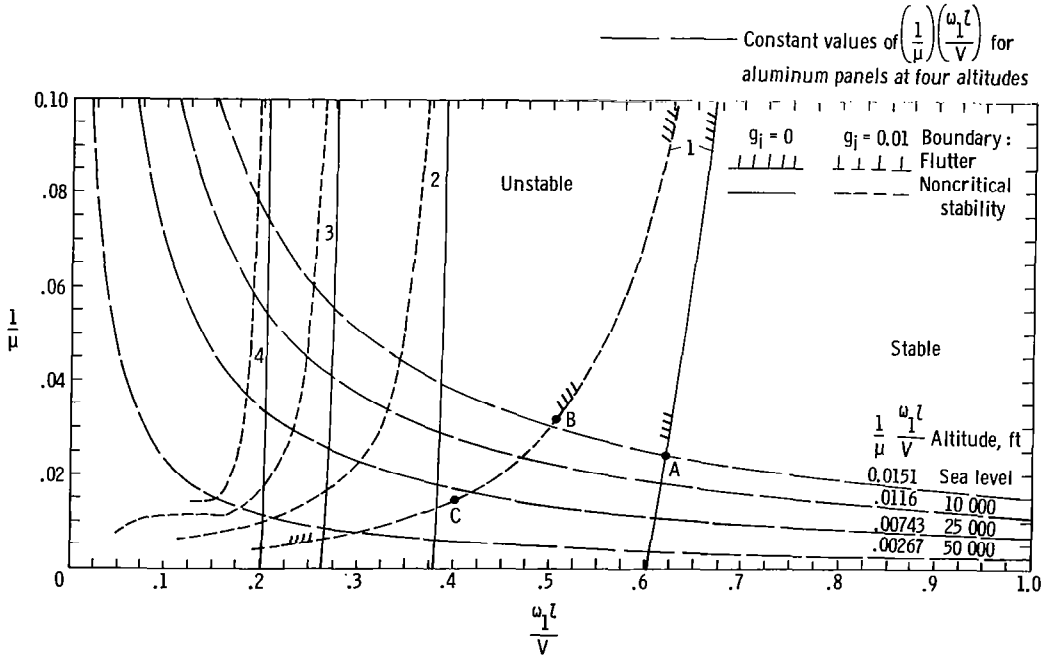

(a) Pinned edges; $\frac{l}{w} = 0$ (two-dimensional case).

Figure 3.- Flutter boundaries and other noncritical stability boundaries for plane, unyawed, unstressed, isotropic, rectangular panels with $M = 1.3$.

$B_S = 40$ and $B_{xs} = 10$, except that $B_{xs} = 1$ for $\frac{l}{w} = 0$. Values of the structural damping coefficient g_i are equal for all modes.

Appendix A gives the expressions for the natural modes from which the values of downwash ratio for each box center and the modal frequencies were computed.

Panels With Simply Supported Edges

Figures 3(a) to 3(g) present the results for the simply supported panels. Figure 3(a) contains portions of the flutter boundary and of three noncritical stability boundaries for the two-dimensional panel $\left(\frac{l}{w} = 0\right)$. The boundaries shown are parts of more complete curves of the type shown in figure 3 of reference 7. The solid curves are the boundaries for $g_i = 0$, and the short-dashed curves are for $g_i = 0.01$. The unstable side of each boundary is to the left. Consequently, the boundary farthest to the right forms the critical or flutter boundary, and is indicated by tick marks on the solid and short-dashed curves. The predominant natural-mode components for the four stability

Quantity	Point A	Point B	Point C
$1/\mu$	0.0301	0.0376	0.0107
g_i	0	0.010	0.010
k_l	0.485	0.405	0.25
$\omega_1 l/V$	0.4974	0.4158	0.2530
ω/ω_1	0.9751	0.974	0.988
q_1	1.0	1.0	1.0
q_2	$(-0.31 + 0.022i) \times 10^{-1}$	$(-0.54 + 0.032i) \times 10^{-1}$	$(-0.41 + 0.013i) \times 10^{-1}$
q_3	$(0.45 - 0.28i) \times 10^{-3}$	$(0.12 - 0.040i) \times 10^{-2}$	$(0.70 - 0.14i) \times 10^{-3}$
q_4	$(-0.72 + 0.059i) \times 10^{-3}$	$(-0.13 + 0.009i) \times 10^{-2}$	$(-0.99 + 0.035i) \times 10^{-3}$
q_5	$(0.26 - 0.21i) \times 10^{-4}$	$(0.70 - 0.29i) \times 10^{-4}$	$(0.41 - 0.10i) \times 10^{-4}$
q_6	$(-0.93 + 0.096i) \times 10^{-4}$	$(-0.16 + 0.015i) \times 10^{-4}$	$(-0.13 + 0.006i) \times 10^{-3}$

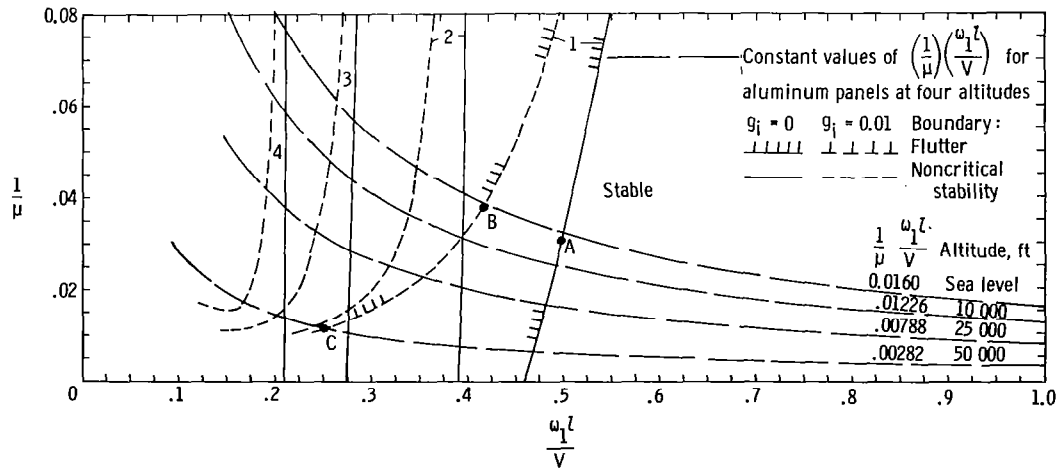

(b) Pinned edges; $\frac{l}{w} = \frac{1}{4}$.

Figure 3.- Continued.

boundaries are given by the numerals 1 to 4. The mode-1 boundary is the critical one for this panel. For the three points labeled by the letters A, B, and C, additional information is given in the table of the figure, including the parameters $1/\mu$, g_i, k_l, $\omega_1 l/V$, ω/ω_1, and the six eigenvector components of the flutter mode. The eigenvectors with their small imaginary parts show that the flutter motion is nearly a standing wave with the shape of the first vacuum mode; that is, the flutter motion is nearly the single degree of freedom described by the first mode.

On figure 3(a) for two-dimensional panels, in addition to the flutter and noncritical stability boundaries, there are four hyperbolas (long-dashed lines) obtained from the U.S. Standard Atmosphere (ref. 8) that apply to aluminum panels at four altitudes, namely, sea level, 10 000, 25 000, and 50 000 feet. The hyperbolas for other altitudes and other panel materials can be determined as desired. The intersection of the appropriate hyperbola with the flutter boundary determines the thickness ratio t/l required to prevent flutter for a given panel material and altitude. For simply supported aluminum panels at sea

Quantity	Point A	Point B	Point C	Point D
$1/\mu$	0.0400	0.0476	0.0150	0.058
g_i	0	0.010	0.010	0
k_l	1.349	1.16	0.90	0.30
$\omega_1 l/V$	0.4069	0.3521	0.2677	0.283
ω/ω_1	3.31	3.30	3.36	1.06
q_1	$(-0.65 + 0.30i) \times 10^{-1}$	$-0.116 + 0.041i$	$(-0.67 + 0.17i) \times 10^{-1}$	1.0
q_2	1.0	1.0	1.0	$-0.26 + 0.025i$
q_3	$(-0.39 + 0.078i) \times 10^{-1}$	$(-0.60 + 0.081i) \times 10^{-1}$	$(-0.31 + 0.021i) \times 10^{-1}$	$(0.23 - 0.05i) \times 10^{-1}$
q_4	$(0.97 + 0.15i) \times 10^{-2}$	$(0.24 - 0.17i) \times 10^{-2}$	$(0.90 - 0.039i) \times 10^{-3}$	<0.01
q_5	$(-0.16 + 0.038i) \times 10^{-2}$	$(-0.25 + 0.044i) \times 10^{-2}$	$(-0.13 + 0.011i) \times 10^{-2}$	<0.01
q_6	$(0.10 - 0.16i) \times 10^{-3}$	$(0.25 - 0.19i) \times 10^{-3}$	$(0.10 - 0.044i) \times 10^{-3}$	<0.001

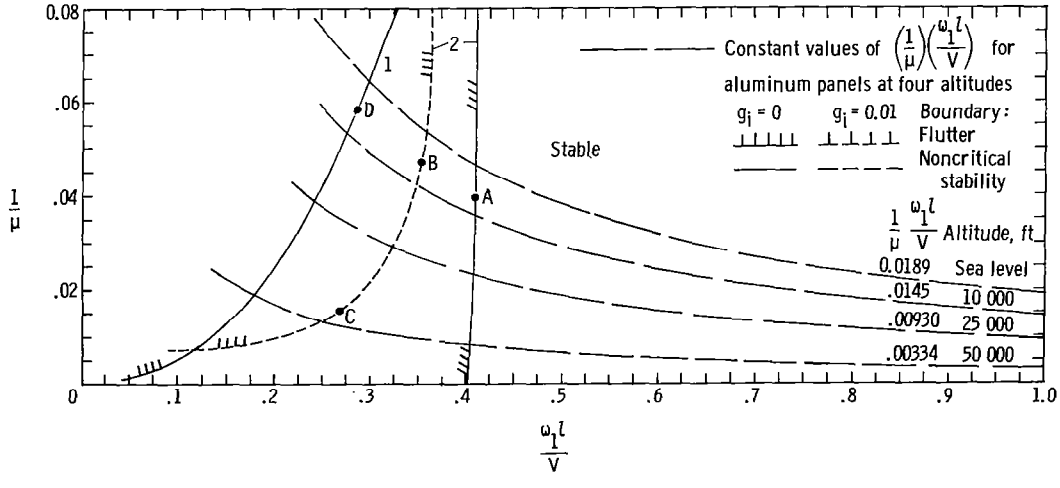

(c) Pinned edges; $\frac{l}{w} = \frac{1}{2}$.

Figure 3.- Continued.

level, the boundary for $g_i = 0$ specifies a minimum thickness ratio of $\frac{t}{l} = 0.0181$, whereas the $g_i = 0.01$ boundary specifies $\frac{t}{l} = 0.0146$. For aluminum panels at 50 000 feet on the $g_i = 0.01$ boundary, $\frac{t}{l} = 0.0087$.

Figure 3(b) gives the results for simply supported panels with $\frac{l}{w} = \frac{1}{4}$. The flutter boundary is predominantly mode 1, that is, nearly a standing wave (see table on fig. 3(b) for points A, B, and C), and the noncritical stability boundaries included are predominantly modes 2, 3, and 4. For aluminum panels at sea level with $g_i = 0$, $\frac{t}{l} = 0.0138$; this value is a 24-percent reduction from the corresponding value for the two-dimensional panel.

Figure 3(c) gives the results for panels with $\frac{l}{w} = \frac{1}{2}$. For the $1/\mu$ range of the figure, the mode-2 boundary is now the flutter boundary for $g_i = 0$ and also for

Quantity	Point A	Point B	Point C	Point D
$1/\mu$	0.0700	0.0548	0.0191	0.0933
g_i	0	0.010	0.010	0
k_l	2.0184	1.8	1.5	0.445
$\omega_1 l/V$	0.4194	0.3715	0.3035	0.325
ω/ω_1	4.80	4.85	4.94	1.37
q_1	$(0.12 - 0.16i) \times 10^{-1}$	$(0.16 - 0.12i) \times 10^{-1}$	$(0.76 - 0.32i) \times 10^{-2}$	1.0
q_2	$-0.11 + 0.062i$	$-0.12 + 0.057i$	$(-0.71 + 0.25i) \times 10^{-1}$	$-0.67 + 0.051i$
q_3	1.0	1.0	1.0	$0.15 - 0.023i$
q_4	$(-0.86 + 0.23i) \times 10^{-1}$	$(-0.85 + 0.17i) \times 10^{-1}$	$(-0.44 + 0.052i) \times 10^{-1}$	$(-0.32 + 0.051i) \times 10^{-1}$
q_5	$(0.37 - 0.54i) \times 10^{-2}$	$(0.44 - 0.40i) \times 10^{-2}$	$(0.16 - 0.10i) \times 10^{-2}$	$(0.10 - 0.018i) \times 10^{-1}$
q_6	$(-0.46 + 0.15i) \times 10^{-2}$	$(-0.47 + 0.11i) \times 10^{-2}$	$(-0.25 + 0.031i) \times 10^{-2}$	$(-0.39 + 0.061i) \times 10^{-2}$

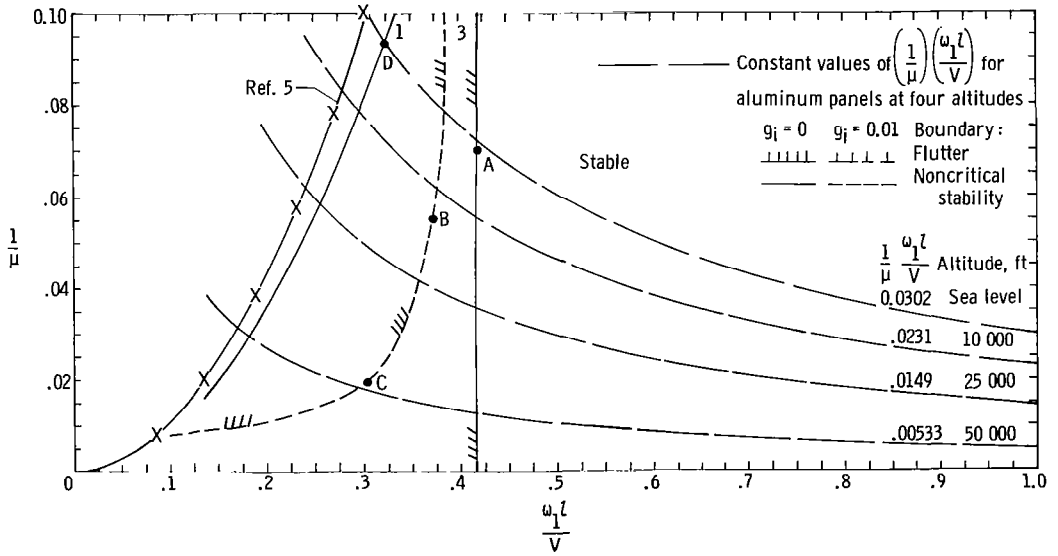

(d) Pinned edges; $\frac{l}{w} = 1$.

Figure 3.- Continued.

$g_i = 0.01$ except in the very lowest range of $1/\mu$. For aluminum panels with $g_i = 0$ at sea level, $\frac{t}{l} = 0.0095$ and is virtually a constant value for all higher altitudes. With $g_i = 0.01$, however, $\frac{t}{l} = 0.0082$ at sea level and decreases to $\frac{t}{l} = 0.0059$ at 50 000 feet. The three points labeled A, B, and C correlate with the quantities given in the table of figure 3(c), and the tabulated values show that the flutter motion is nearly a single-degree-of-freedom standing wave in the second natural mode. Point B corresponding to the higher air density contains the larger components of modes 1 and 3, and these components are so phased that the aft portion of the panel has a slightly larger amplitude than the forward half of the panel. The mode-1 stability boundary, labeled with the numeral 1, is no longer the critical boundary unless g_i should become as large as about 0.03. In figure 3(c) the character of the mode-1 boundary for $g_i = 0$ (the boundary for $g_i = 0.01$ is virtually coincident) is entirely different from those of figures 3(a) and 3(b).

Quantity	Point A	Point B	Point C	Point D
$1/\mu$	0.1269	0.12	0.0707	0.0210
g_j	0	0	0.010	0.010
k_l	0.68	3.337	3.0	2.8
$\omega_1 l/V$	0.5926	0.603	0.5324	0.3521
ω/ω_1	1.147	5.53	5.63	7.95
q_1	1.0	$(0.63 - 0.79i) \times 10^{-2}$	$(0.48 - 0.44i) \times 10^{-2}$	$(-0.23 + 0.004i) \times 10^{-2}$
q_2	$-0.93 + 0.16i$	$(-0.26 + 0.13i) \times 10^{-1}$	$(-0.20 + 0.069i) \times 10^{-1}$	$(0.23 - 0.082i) \times 10^{-2}$
q_3	$0.34 - 0.10i$	$(0.34 - 0.33i) \times 10^{-1}$	$(0.26 - 0.16i) \times 10^{-1}$	$(-0.93 + 0.25i) \times 10^{-2}$
q_4	$(-0.91 + 0.28i) \times 10^{-1}$	$-0.20 + 0.11i$	$-0.16 + 0.078i$	$(0.70 + 0.24i) \times 10^{-2}$
q_5	$(0.31 - 0.097i) \times 10^{-1}$	1.0	1.0	$(-0.91 + 0.20i) \times 10^{-1}$
q_6	$(-0.13 + 0.036i) \times 10^{-1}$	$-0.17 + 0.057i$	$-0.13 + 0.034i$	1.0
q_7		$(0.14 - 0.17i) \times 10^{-1}$	$(0.94 - 0.88i) \times 10^{-2}$	$(-0.66 + 0.074i) \times 10^{-1}$
q_8		$(-0.13 + 0.052i) \times 10^{-1}$	$(-0.98 + 0.27i) \times 10^{-2}$	$(0.31 - 0.15i) \times 10^{-2}$
q_9		$(0.24 - 0.30i) \times 10^{-2}$	$(0.16 - 0.16i) \times 10^{-2}$	$(-0.51 + 0.053i) \times 10^{-2}$
q_{10}		$(-0.30 + 0.13i) \times 10^{-2}$	$(-0.23 + 0.68i) \times 10^{-2}$	$(0.60 - 0.29i) \times 10^{-3}$
q_{11}		$(0.72 - 0.93i) \times 10^{-3}$	$(0.51 - 0.48i) \times 10^{-3}$	$(-0.13 + 0.014i) \times 10^{-2}$
q_{12}		$(-0.10 + 0.046i) \times 10^{-2}$	$(-0.82 + 0.24i) \times 10^{-3}$	$(0.19 - 0.092i) \times 10^{-3}$

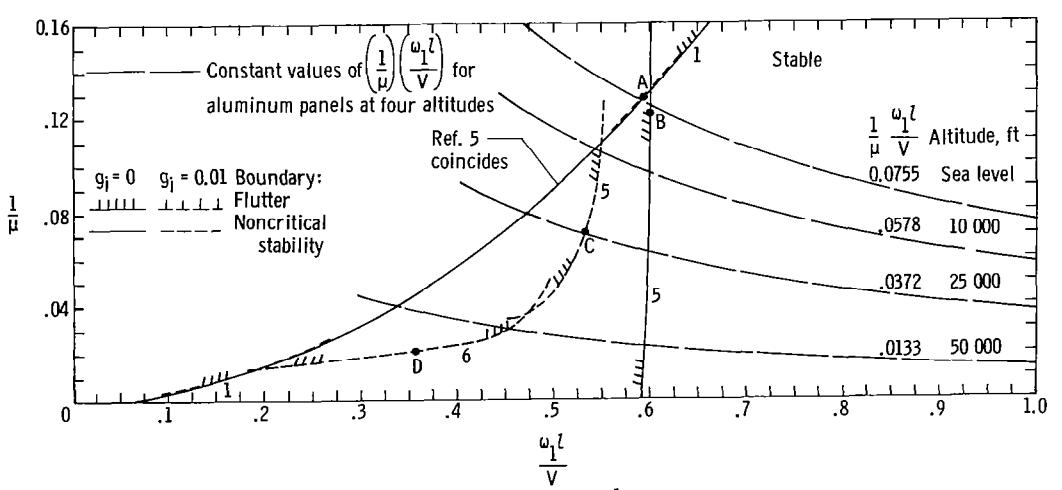

(e) Pinned edges; $\frac{l}{w} = 2$.

Figure 3.- Continued.

Instead of intersecting the horizontal axis, it departs from the origin in the manner of a near parabola.

Figure 3(d) gives the results for panels with $\frac{l}{w} = 1$. The mode-3 boundary now forms the flutter boundary for $g_i = 0$ and $g_i = 0.01$, and the flutter mode is predominantly the third natural mode (see points A, B, and C and the table), small proportions of modes 2 and 4 being present. If the structural damping coefficient could somehow be as large as about 0.03, the mode-1 boundary would become the flutter boundary since it is of the type that is only slightly affected by an increase of g_i to 0.03. The flutter motion for the mode-1 boundary is characterized by having the natural mode 1 predominate, having a large proportion of mode 2 present, and having the proportions of the higher modes decrease. Refer to point D on figure 3(d) and its column in the table. The motion is nearly a standing wave, as evidenced by the small imaginary parts of the generalized coordinates, and the aft part of the panel has a substantially larger amplitude than the forward part. For aluminum panels at sea level with $g_i = 0$, $\frac{t}{l} = 0.0060$, and for $g_i = 0.01$, $\frac{t}{l} = 0.0056$. The parabolic boundary obtained from equation (9) of reference 5 is included as a matter of interest and it is observed to fall close to the flutter boundary of the present analysis for $g_i \approx 0.03$.

Figure 3(e) gives the results for panels with $\frac{l}{w} = 2$. With $g_i = 0$ the mode-5 boundary is critical for most of the range of $1/\mu$ (less than about 0.13), and the mode-1 boundary is critical for higher values of $1/\mu$. With $g_i = 0.01$, the numbers labeling the segments of short-dashed curves show that the mode-1 boundary is critical for the high and low ranges of $1/\mu$. In the intermediate range of $1/\mu$, the flutter boundary is formed partly by the mode-6 boundary and partly by the mode-5 boundary. The associated tabulated values show that at point A on the mode-1 boundary, the flutter motion is strongly coupled; natural modes 1 and 2 are present in nearly equal parts, natural mode 3 is present in a significant amount, and the other modes are present in small amounts. The mode-1 boundary of figure 3(e) has this characteristic throughout the range of $1/\mu$ of the figure. At points B and C on the mode-5 boundary and point D on the mode-6 boundary, the motion is dominated by the respective natural mode, moderate to small amounts of other modes being present. For aluminum panels at sea level with $g_i = 0$, $\frac{t}{l} = 0.0035$ (mode-5 boundary) and with $g_i = 0.01$, $\frac{t}{l} = 0.0034$ (mode-1 boundary). The parabolic boundary from equation (9) of reference 5 is so closely coincident to the mode-1 boundary that it is not drawn.

Figure 3(f) displays the results for panels with $\frac{l}{w} = 4$. With $g_i = 0$, the flutter boundary is formed, beginning at the lowest value of $1/\mu$, by segments of the mode-8, the mode-9, and the mode-2 boundaries. With $g_i = 0.01$, the flutter boundary is made up of segments of the mode-2, the mode-12, the mode-11, the mode-10, and the mode-2 boundaries. On the mode-2 boundary, as indicated by the tabulated values for point A, the

flutter motion contains large components of several of the natural modes, the mode-2 component being the largest. The imaginary parts of the components indicate that the flutter motion is not (even approximately) a standing wave. On the other boundary segments labeled 8, 9, 10, 11, and 12, those respective natural modes are predominant in the flutter motion with moderate to small proportions of other modes being present for points B, C, D, and E as indicated in the table of figure 3(f). For aluminum panels at sea level, $\frac{t}{l} = 0.0020$ for both $g_i = 0$ and $g_i = 0.01$, since the mode-2 boundary is not significantly affected by structural damping. In figure 3(f) the parabolic boundary from equation (9) of reference 5 falls near the mode-2 boundary and on the conservative side and calls for a greater thickness to prevent flutter

Figure 3(g) shows the results for panels with $\frac{l}{w} = 10$. The flutter boundary is formed by the mode-7 boundary throughout the range of $1/\mu$ shown. For aluminum panels at sea level, the flutter boundary corresponds to $\frac{t}{l} = 0.00097$ for $g_i = 0$ and to $\frac{t}{l} = 0.00096$ for $g_i = 0.01$. The mode-9 boundary (natural modes 3 to 14 used in the analysis) and the mode-11 boundary (natural modes 5 to 16 used in the analysis) are in the unstable region very close to the flutter boundary. Stability boundaries associated with modes 2, 4, and 6 (not shown) also lie within the unstable region, the mode-2 boundary being the farthest from the flutter boundary. For the three points A, B, and C on the flutter boundary, parameters and generalized coordinates are given in the table of figure 3(g). The value of q_{12} is markedly larger than that for any other boundary in figure 3 (except, of course, the mode-12 and mode-11 boundaries of figure 3(f). This large value of q_{12} leads naturally to the question of whether 12 modes are sufficient in this particular modal solution to provide a substantially converged result. Therefore, spot checks were made with 18 modes. Since more than 12 modes could be used only outside the main program and the required intermediate work was extensive, spot checks were made for only two values of reduced frequency. With 18 modes the flutter boundary moved inward to the left by an amount that would reduce the thickness required to prevent flutter by about 8 percent. The mode-7 boundary still formed the flutter boundary, and other stability boundaries also moved and maintained their relative locations. At the two widely separated points obtained on the mode-7 flutter boundary (see the last 2 columns in table of fig. 3(g)), the generalized coordinates decreased monotonically for the modes above q_7. For the 18th mode, $|q_{18}| \approx 0.02$, whereas for mode 12, $|q_{12}| \approx 0.14$. The result is, therefore, thought to be substantially converged, although rigorous proof is lacking. The parabola of long dashes from equation (9) of reference 5 corresponding to a value of $\lambda = 51\ 390$ is close to the flutter boundary of the present analysis. The associated flutter frequency ratio $\frac{\omega}{\omega_1} \approx 1.18$ and falls just above the fourth natural mode $\frac{\omega}{\omega_1} \approx 1.15$.

Additional information for this panel is given by figure 4 that presents the flutter mode shapes as obtained from the present analysis and from an automated solution of

Quantity	Point A	Point B	Point C	Point D	Point E
$1/\mu$	0.218	0.133	0.0710	0.0580	0.0440
g_j	0	0	0.010	0.010	0.010
k_ℓ	1.26	6.15	6.2	7.0	7.0
$\omega_1 \ell / V$	1.163	1.114	0.9231	0.8792	0.7491
ω / ω_1	1.083	5.51	6.72	7.97	9.35
q_1	-0.74 - 0.20i				
q_2	1.0				
q_3	-0.71 + 0.16i	$(0.40 - 0.56i) \times 10^{-2}$	$(-0.33 + 1.0i) \times 10^{-2}$	$(0.93 - 0.87i) \times 10^{-3}$	
q_4	0.35 - 0.12i	$(-0.98 + 0.66i) \times 10^{-2}$	$(0.27 - 0.22i) \times 10^{-2}$	$(-0.26 + 0.093i) \times 10^{-2}$	
q_5	-0.16 + 0.055i	$(0.92 + 1.20i) \times 10^{-2}$	$(-0.69 + 0.28i) \times 10^{-2}$	$(0.20 - 0.15i) \times 10^{-2}$	$(-0.24 + 0.071i) \times 10^{-2}$
q_6	$(0.73 - 0.25i) \times 10^{-1}$	$(-0.26 + 0.19i) \times 10^{-1}$	$(0.60 - 0.39i) \times 10^{-2}$	$(-0.53 + 0.22i) \times 10^{-2}$	$(0.18 - 0.081i) \times 10^{-2}$
q_7	$(-0.36 + 0.12i) \times 10^{-1}$	$(0.32 - 0.38i) \times 10^{-1}$	$(-0.18 + 0.087i) \times 10^{-1}$	$(0.44 - 0.26i) \times 10^{-2}$	$(-0.46 + 0.18i) \times 10^{-2}$
q_8	$(0.19 - 0.61i) \times 10^{-1}$	-0.21 + 0.14i	$(0.21 - 0.089i) \times 10^{-1}$	$(-0.13 + 0.068i) \times 10^{-1}$	$(0.38 - 0.12i) \times 10^{-2}$
q_9	$(-0.11 + 0.034i) \times 10^{-1}$	1.0	-0.16 + 0.075i	$(0.15 - 0.052i) \times 10^{-1}$	$(-0.12 + 0.062i) \times 10^{-1}$
q_{10}	$(0.64 - 0.19i) \times 10^{-2}$	-0.20 + 0.088i	1.0	-0.12 + 0.065i	$(0.84 + 0.011i) \times 10^{-2}$
q_{11}	$(-0.40 + 0.12i) \times 10^{-2}$	$(0.17 - 0.27i) \times 10^{-1}$	-0.14 + 0.044i	1.0	-0.11 + 0.037i
q_{12}	$(-0.27 - 0.079i) \times 10^{-2}$	$(0.34 - 0.58i) \times 10^{-2}$	$(0.097 - 0.10i) \times 10^{-1}$	-0.10 + 0.036i	1.0
q_{13}		$(-0.50 + 0.28i) \times 10^{-2}$	$(-0.13 + 0.042i) \times 10^{-1}$	$(0.61 - 0.73i) \times 10^{-2}$	-0.096 + 0.023i
q_{14}			$(0.21 - 0.24i) \times 10^{-2}$	$(-0.99 + 0.33i) \times 10^{-2}$	$(0.55 - 0.44i) \times 10^{-2}$
q_{15}					$(-0.89 + 0.20i) \times 10^{-2}$
q_{16}					$(0.13 - 0.11i) \times 10^{-2}$

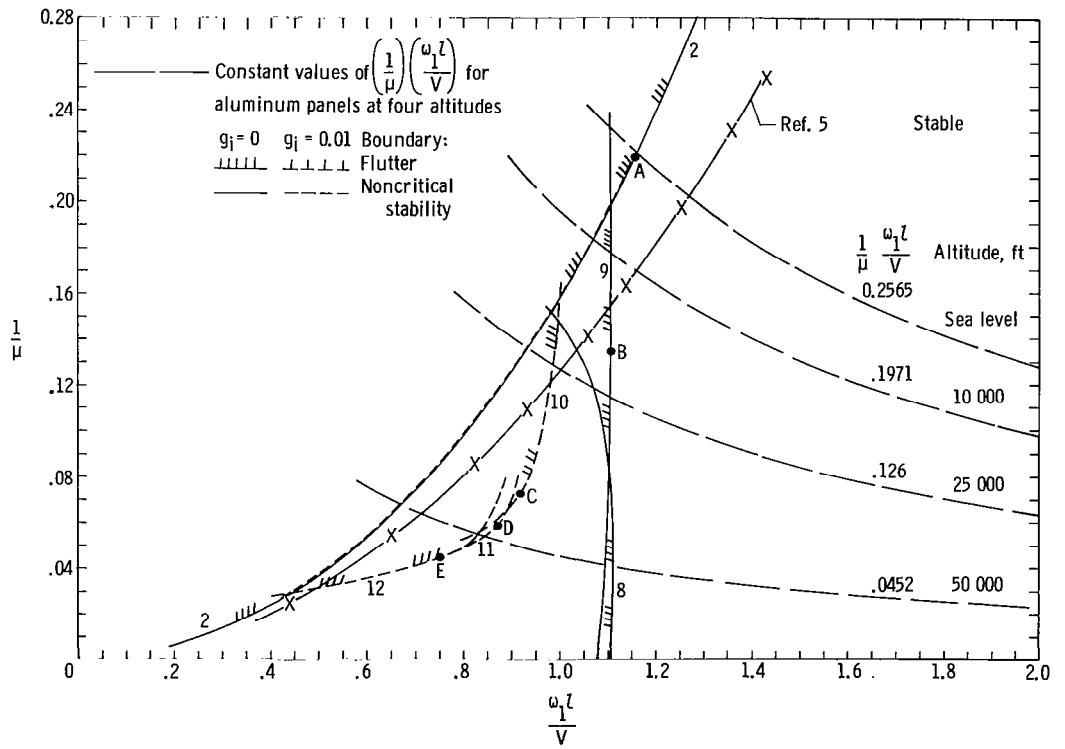

(f) Pinned edges; $\frac{\ell}{w} = 4$.

Figure 3.- Continued.

Quantity	Point A	Point B	Point C	*	*
$1/\mu$	0.464	0.302	0.174	0.662	0.057
g_i	0	0	0	0	0
k_l	4.5	3.8	3.0	4.5	1.5
$\omega_1 l/V$	3.415	2.825	2.20	3.52	1.13
ω/ω_1	1.3177	1.344	1.37	1.28	1.33
q_1	0.052 - 0.00015i	0.047 - 0.00088i	0.043 - 0.00079i	0.10 + 0.015i	0.073 + 0.0020i
q_2	-0.111 - 0.0022i	-0.099 + 0.00026i	-0.092 + 0.00078i	-0.21 - 0.033i	-0.16 - 0.0046i
q_3	0.19 + 0.0078i	0.17 + 0.0022i	0.16 + 0.00066i	0.33 + 0.057i	0.26 + 0.0088i
q_4	-0.30 - 0.027i	-0.28 - 0.014i	-0.26 - 0.0078i	-0.48 - 0.089i	-0.40 - 0.016i
q_5	0.48 + 0.062i	0.45 + 0.038i	0.42 + 0.024i	0.67 + 0.12i	0.60 + 0.026i
q_6	-0.74 - 0.11i	-0.73 - 0.080i	-0.71 + 0.057i	-0.87 - 0.12i	-0.85 - 0.029i
q_7	1.0	1.0	1.0	1.0	1.0
q_8	-0.81 + 0.23i	-0.83 + 0.19i	-0.85 + 0.15i	-0.88 + 0.17i	-0.85 + 0.041i
q_9	0.44 - 0.21i	0.45 - 0.17i	0.47 - 0.13i	0.60 - 0.21i	0.55 - 0.043i
q_{10}	-0.25 + 0.13i	-0.26 + 0.10i	-0.26 + 0.076i	-0.38 + 0.16i	-0.33 + 0.028i
q_{11}	0.15 - 0.074i	0.14 - 0.057i	0.15 - 0.041i	0.24 - 0.11i	0.20 - 0.017i
q_{12}	-0.11 + 0.058i	-0.11 + 0.043i	-0.11 + 0.031i	-0.15 + 0.070i	-0.13 + 0.010i
q_{13}				0.10 - 0.045i	0.083 - 0.0063i
q_{14}				-0.071 + 0.031i	-0.057 + 0.0043i
q_{15}				0.050 - 0.021i	0.040 - 0.0025i
q_{16}				-0.037 + 0.015i	-0.029 + 0.0037i
q_{17}				0.027 - 0.010i	0.021 + 0.00036i
q_{18}				-0.022 + 0.0087i	-0.017 - 0.00026i

*Discussed in text only.

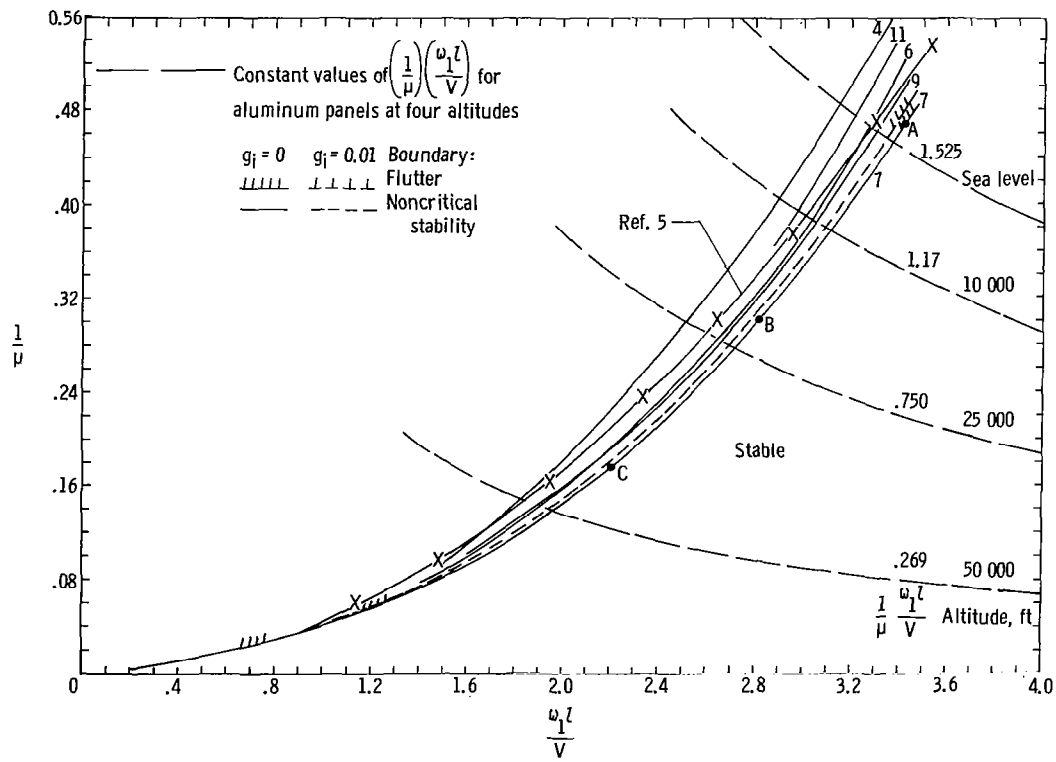

(g) Pinned edges; $\frac{l}{w} = 10$.

Figure 3.- Concluded.

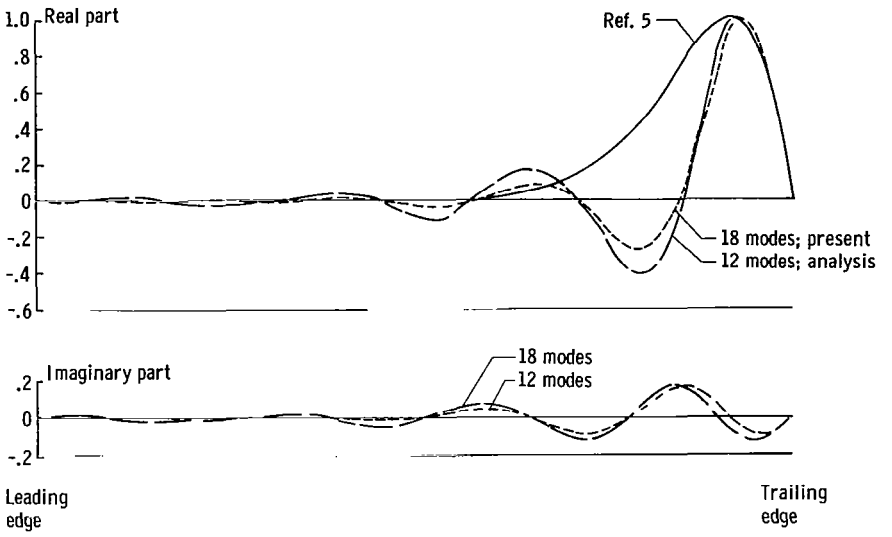

Figure 4.- Flutter mode shapes from present analysis with 12 and with 18 modes, M = 1.3, and k_l = 4.5, and from equation (9) of reference 5 for a simply supported rectangular panel with l/w = 10, g_j = 0.

equation (9) of reference 5. The latter result is real only and is associated with the point at a length-width ratio of 10 on the solid curve of figure 2 of reference 4. From the present analysis, both the real (inphase) and imaginary (quadrature) parts as obtained from using 12 modes and also from using 18 modes are shown. The two results are for k_l = 4.5. The 12-mode result corresponds to point A in figure 3(g) and the first column of the table. The 18-mode result corresponds to the tabulated column second from the right. An examination of those two columns and the corresponding pairs of curves of figure 4 reveals their moderate differences. The closed-form solution based on reference 5 is like the solutions from the present analysis in that the point of maximum deflection is at about 93 percent of the panel length, and very little motion occurs over the forward half of the panel; the solution differs in that the signs forward of the maximum deflection point do not alternate. A Fourier analysis, with 101 points and $0 \leqq n \leqq 50$, of the closed-form deflection curve has given the results of table II. The largest proportion present is for $p = 3$ half-waves, a gradual and monotonic decrease of proportions for p increasing above 3; and there is an unfailing alternation of sign for even and odd p. The proportions of sine waves in table II can be compared with the generalized coordinates in the columns of the table in figure 3(g).

Panels With Clamped Edges

Figures 5(a) to 5(f) present the results for clamped-edge panels. In each of the six figures the solid curve with tick marks attached is the flutter boundary for $g_i = 0$, and

TABLE II.- PROPORTIONS OF SINE WAVES WITH n HALF-WAVES PRESENT IN THE DEFLECTION SHAPE LABELED "REF. 5" IN FIGURE 4

Number of half-waves, n	Proportions present
0	0
1	.544
2	-.901
3	1.000
4	-.905
5	.722
6	-.536
7	.382
8	-.267
9	.186
10	-.130
11	.0923
12	-.0660
13	.0478
14	-.0351
15	.0261
16	-.0196
17	.0149
18	-.0115
19	.00895
.	.
.	.
.	.
49	.0000580
50	-.0000507

the curve of short dashes with tick marks is the flutter boundary for $g_i = 0.01$. The flutter region is to the left of the flutter boundary in all the figures. In addition to the flutter boundary, some of the noncritical stability boundaries that also result from the eigensolution are shown without tick marks so that the progressive alteration of the flutter boundary with increasing values of l/w can be more readily appreciated. Also given in each figure are the hyperbolas that apply to aluminum panels at sea level and at 10 000, 25 000, and 50 000 feet in a standard atmosphere (ref. 8). In figures 5(d) to 5(f) with $\frac{l}{w} \geqq 1.0$, the closed-form solutions based on the Ackeret value of static aerodynamic forces are also

presented as the labeled parabolas. The solutions were obtained essentially as described in reference 6 except for the minor differences that (1) the cross-stream variation of mode shape was assumed to be the natural vibration mode of a uniform clamped-end beam with a single half-wave instead of a 1.0-minus-cosine type of half-wave (see eq. (8.37) of ref. 6), and (2) the dynamic pressure parameter λ was defined as in reference 5 as $\lambda = \frac{2q\ell^3}{\beta D}$ and is consistent with the assumed aerodynamic forces.

Figure 5(a) applies to $\frac{\ell}{w} = 0$ (the two-dimensional case) and the solid lines shown are essentially identical to portions of those from figure 3 of reference 7. The predominant modes are indicated by the number for each boundary. For the three points labeled by the letters A, B, and C on the flutter boundaries, information is given in the table. Clearly, the flutter mode is virtually a standing wave with a small amount of the second natural mode present along with the predominant first natural mode. For aluminum panels at sea level, the thickness ratio for $g_i = 0$ is $\frac{t}{\ell} = 0.0098$, and for $g_i = 0.01$,

Quantity	Point A	Point B	Point C
$1/\mu$	0.0441	0.0527	0.01087
g_i	0	0.010	0.010
k_ℓ	0.745	0.66	0.40
$\omega_1\ell/V$	0.7583	0.6690	0.4007
ω/ω_1	0.982	0.987	0.998
q_1	1.0	1.0	1.0
q_2	-0.050 + 0.0046i	-0.077 + 0.0058i	-0.042 + 0.0012i
q_3	(0.13 - 0.093i) × 10^{-2}	(0.28 - 0.11i) × 10^{-2}	(0.89 - 0.17i) × 10^{-3}
q_4	(-0.12 + 0.024i) × 10^{-2}	(-0.18 + 0.030i) × 10^{-2}	(-0.10 + 0.005i) × 10^{-2}
q_5	(0.90 - 0.91i) × 10^{-4}	(0.18 - 0.11i) × 10^{-3}	(0.61 - 0.15i) × 10^{-2}
q_6	(-0.13 + 0.037i) × 10^{-3}	(-0.21 + 0.045i) × 10^{-3}	(-0.11 + 0.006i) × 10^{-3}

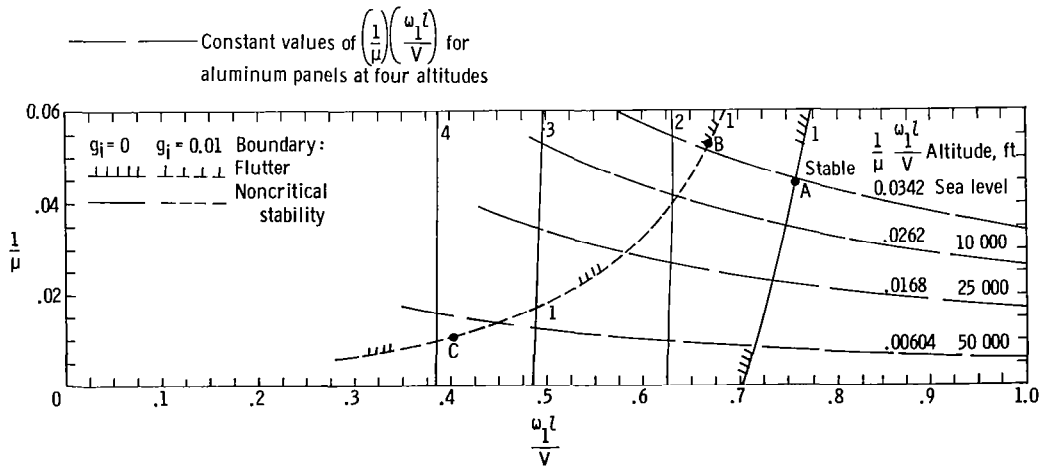

(a) Clamped edges; $\frac{\ell}{w} = 0$ (two-dimensional case).

Figure 5.- Flutter boundaries and other noncritical stability boundaries for plane, unyawed, unstressed, isotropic, rectangular panels with M = 1.3.

$\frac{t}{l} = 0.0086$. For aluminum panels at 50 000 feet on the $g_i = 0.01$ flutter boundary, $\frac{t}{l} = 0.0058$.

Figure 5(b) applies to $\frac{l}{w} = \frac{1}{4}$. When compared with figure 5(a), the unstable region has shrunk, the mode-1 boundary having moved to the left considerably more than the mode-2 boundary has. The result is that in the lower range of $1/\mu$, the mode-2 boundary forms the flutter boundary for both $g_i = 0$ and $g_i = 0.01$. As indicated in the table of figure 5(b), points A and B are predominantly mode 1, some mode 2 being present; and point C is predominantly mode 2, small amounts of modes 1 and 3 being present. For aluminum panels at sea level, $\frac{t}{l} = 0.0081$ for $g_i = 0$, and $\frac{t}{l} = 0.0070$ for $g_i = 0.01$.

Figure 5(c) applies to $\frac{l}{w} = \frac{1}{2}$. For $g_i = 0$ the mode-2 boundary forms the flutter boundary throughout the $1/\mu$ range shown. For $g_i = 0.01$, the mode-2 boundary is critical for about $0.01 < 1/\mu < 0.10$. The parameters listed for points A, B, C, and D show that the flutter mode is predominantly natural mode 2 and has small to moderate amounts of modes 1 and 3. The amounts of modes 1 and 3 that are present increase with increasing values of $1/\mu$. The mode-1 boundary has changed its character from that for

Quantity	Point A	Point B	Point C
$1/\mu$	0.0566	0.06173	0.0192
g_i	0	0.010	0.010
K_l	0.635	0.575	1.2
$\omega_1 l/V$	0.6475	0.5790	0.4447
ω/ω_1	0.981	0.993	2.70
q_1	1.0	1.0	-0.063 + 0.018i
q_2	-0.091 + 0.0070i	-0.12 + 0.0086i	1.0
q_3	(0.37 - 0.16i) × 10^{-2}	(0.64 - 0.20i) × 10^{-2}	-0.036 + 0.0021i
q_4	(-0.22 + 0.040i) × 10^{-2}	(-0.31 + 0.050i) × 10^{-2}	(0.12 - 0.058i) × 10^{-2}
q_5	(0.23 - 0.14i) × 10^{-3}	(0.41 - 0.18i) × 10^{-3}	(-0.15 + 0.023i) × 10^{-2}
q_6	(-0.24 + 0.061i) × 10^{-3}	(-0.35 + 0.073i) × 10^{-3}	(0.15 - 0.087i) × 10^{-3}

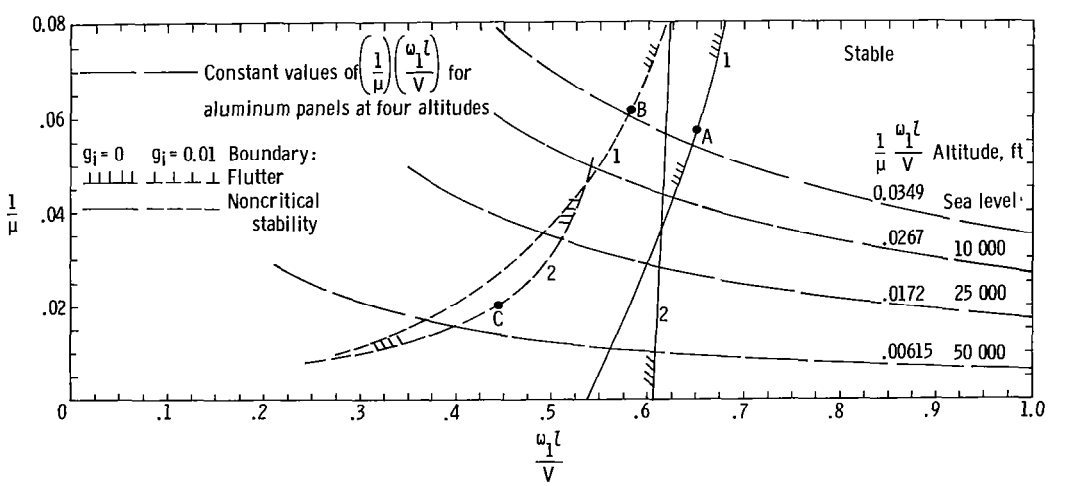

(b) Clamped panel; $\frac{l}{w} = \frac{1}{4}$.

Figure 5.- Continued.

$\frac{l}{w} = \frac{1}{4}$ and 0; in figure 5(c) it is approximately a parabola with its apex at the origin. Furthermore, the flutter mode is a coupled one, mainly of modes 1 and 2, formed by a near coalescence of those two flow-affected frequencies. If g_i should be greater than 0.03, the mode-1 boundary is the flutter boundary for the range of $1/\mu$ of the figure. For aluminum panels at sea level, $\frac{t}{l} = 0.0068$ for $g_i = 0$, and $\frac{t}{l} = 0.0059$ for $g_i = 0.01$.

Figure 5(d) applies to $\frac{l}{w} = 1$. For $g_i = 0$ the mode-3 boundary forms the flutter boundary in the $1/\mu$ range shown. For $g_i = 0.01$, the flutter boundary is formed by the mode-1, -3, and -4 stability boundaries. For g_i greater than about 0.03, the mode-1 boundary is the flutter boundary. For the five points labeled A to E on the flutter boundaries, the proportions of the first six natural modes are given in the table of figure 5(d).

Quantity	Point A	Point B	Point C	Point D	Point E
$1/\mu$	0.0725	0.0775	0.0370	0.0120	0.0828
g_i	0	0.010	0.010	0.010	0
k_l	1.46	1.25	1.2	0.8	0.5
$\omega_1 l/V$	0.5833	0.5022	0.471	0.3101	0.4651
ω/ω_1	2.50	2.48	2.55	2.58	1.075
q_1	-0.14 + 0.050i	-0.22 + 0.059i	-0.12 + 0.034i	-0.094 + 0.016i	1.0
q_2	1.0	1.0	1.0	1.0	-0.30 + 0.018i
q_3	-0.089 + 0.015i	-0.12 + 0.014i	-0.069 + 0.0073i	-0.049 + 0.0017i	0.034 - 0.0060i
q_4	$(0.49 - 0.44i) \times 10^{-2}$	$(0.95 - 0.47i) \times 10^{-2}$	$(0.35 - 0.20i) \times 10^{-2}$	$(0.19 - 0.042i) \times 10^{-2}$	$(-0.90 + 0.15i) \times 10^{-2}$
q_5	$(-0.36 + 0.14i) \times 10^{-2}$	$(-0.55 + 0.14i) \times 10^{-2}$	$(-0.30 + 0.62i) \times 10^{-2}$	$(-0.21 + 0.014i) \times 10^{-2}$	$(0.21 - 0.058i) \times 10^{-2}$
q_6	$(0.47 - 0.58i) \times 10^{-3}$	$(0.96 - 0.64i) \times 10^{-3}$	$(0.38 - 0.28i) \times 10^{-3}$	$(0.21 - 0.058i) \times 10^{-3}$	$(-0.10 + 0.023i) \times 10^{-2}$

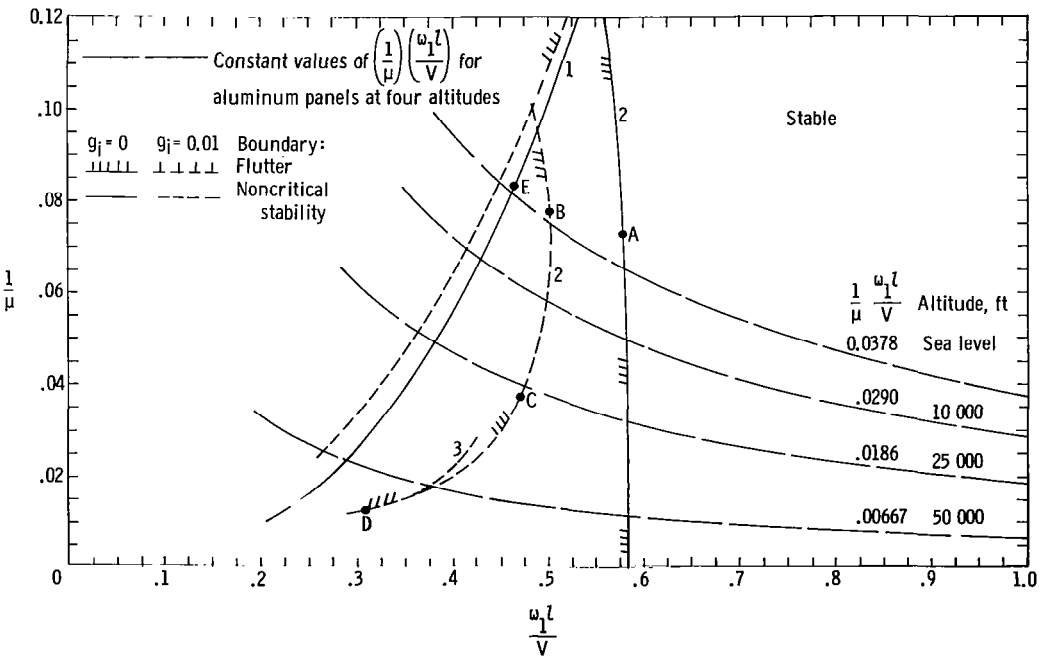

(c) Clamped panel; $\frac{l}{w} = \frac{1}{2}$.

Figure 5.- Continued.

The mode-1 boundary is characterized by a strongly coupled motion. (See point A.) The other boundaries each have a predominant mode, moderate to small proportions of adjacent modes being present. For aluminum panels at sea level, $\frac{t}{l} = 0.0048$ for $g_i = 0$, and $\frac{t}{l} = 0.0043$ for $g_i = 0.01$. The parabolic boundary from the closed-form solution is included and falls on the unconvervative side of the mode-1 boundary.

Figure 5(e) applies to $\frac{l}{w} = 2$. For $g_i = 0$, the flutter boundary is formed by the mode-1 and the mode-5 boundaries, the mode-6 and mode-7 boundaries being near the

Quantity	Point A	Point B	Point C	Point D	Point E
$1/\mu$	0.0966	0.1104	0.0940	0.0436	0.0163
g_i	0	0.010	0.010	0.010	0.010
kl	2.12	0.628	2.96	1.8	2.1
$\omega_1 l/V$	0.6050	0.5188	0.5249	0.502	0.3606
ω/ω_1	3.50	1.21	5.63	3.59	5.82
q_1	0.032 - 0.018i	1.0	-0.013 + 0.0025i	0.019 - 0.0063i	$(-0.34 - 0.073i) \times 10^{-2}$
q_2	-0.19 + 0.082i	-0.64 + 0.068i	0.029 - 0.016i	-0.13 + 0.049i	$(0.73 + 0.36i) \times 10^{-2}$
q_3	1.0	0.16 - 0.034i	-0.15 + 0.087i	1.0	-0.068 + 0.016i
q_4	-0.14 + 0.032i	-0.032 + 0.0090i	1.0	-0.091 + 0.014i	1.0
q_5	0.011 - 0.011i	$(0.99 - 0.32i) \times 10^{-2}$	-0.13 + 0.035i	$(0.58 - 0.42i) \times 10^{-2}$	-0.044 + 0.0026i
q_6	$(-0.74 + 0.32i) \times 10^{-2}$	$(-0.34 + 0.12i) \times 10^{-2}$	0.0010 - 0.012i	$(-0.50 + 0.13i) \times 10^{-2}$	$(0.21 - 0.071i) \times 10^{-2}$

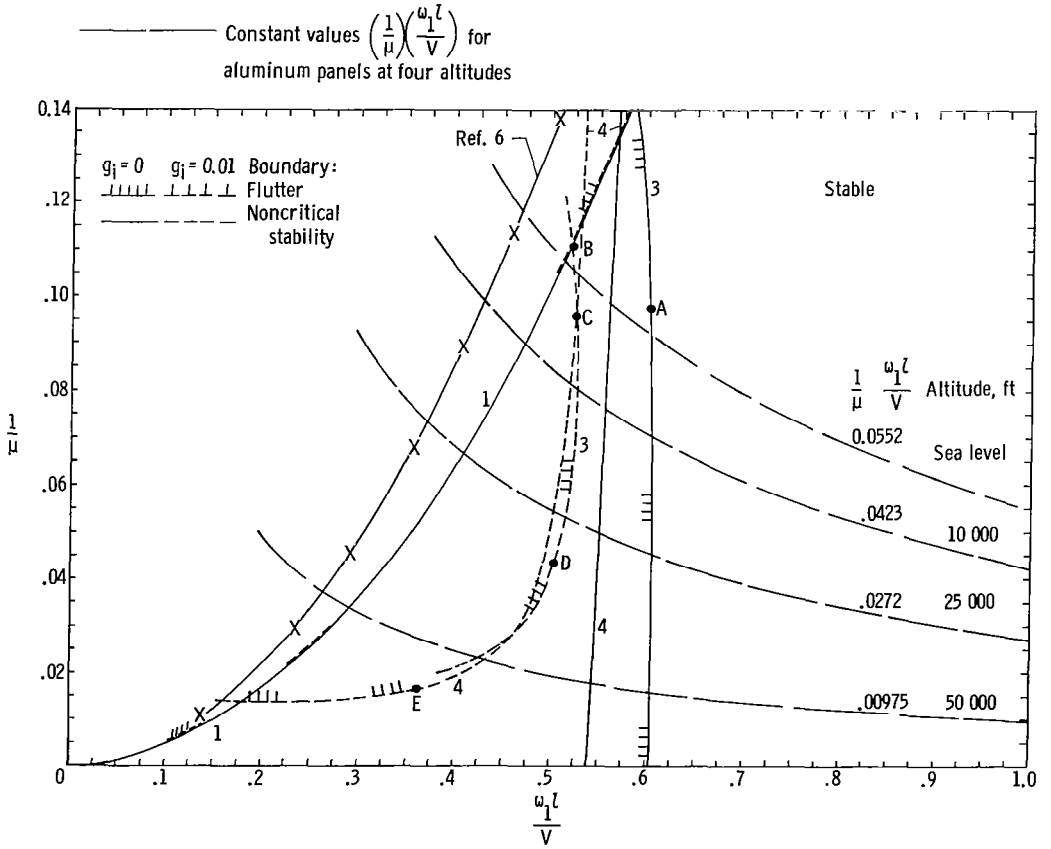

(d) Clamped panel; $\frac{l}{w} = 1$.

Figure 5.- Continued.

mode-5 boundary. For $g_i = 0.01$, the flutter boundary is formed by portions of the mode-1, -6, -7, and -8 stability boundaries. (The mode-7 and -8 boundaries are virtually coincident over part of the range.) For g_i as large as about 0.03, the mode-1 boundary is the flutter boundary. The parameters listed included the eigenvectors for point A (coupled motion) and also for points B, C, D, and E where one mode is predominant for each. For aluminum panels at sea level, $\frac{t}{l} = 0.0031$ for both $g_i = 0$ and 0.01. The parabolic boundary from the closed-form solution falls close to the mode-1 boundary.

Figure 5(f) applies to $\frac{l}{w} = 4$. For $g_i = 0$, the flutter boundary is formed by portions of the mode-2, the mode-10, and the mode-9 stability boundaries. The mode-11 and mode-12 boundaries (and other higher mode boundaries not shown) lie to the left of the

Quantity	Point A	Point B	Point C	Point D	Point E
$1/\mu$	0.1398	0.0753	0.0400	0.0280	0.0274
g_i	0	0	0.010	0.010	0.010
k_l	1.12	3.4	3.6	4.8	3.6
$\omega_1 l/V$	1.063	0.9829	0.768	0.624	0.590
ω/ω_1	1.053	3.46	4.69	7.69	6.10
q_1	1.0	$(0.38 - 0.33i) \times 10^{-2}$	$(-0.17 - 0.046i) \times 10^{-2}$	$(-0.43 - 0.13i) \times 10^{-3}$	$(0.45 - 0.42i) \times 10^{-3}$
q_2	$-0.88 + 0.24i$	$-0.015 + 0.0036i$	$(0.30 - 0.13i) \times 10^{-2}$	$(0.53 - 0.25i) \times 10^{-3}$	$(-2.1 - 0.15i) \times 10^{-3}$
q_3	$0.29 - 0.15i$	$0.027 - 0.014i$	$(-1.0 + 0.20i) \times 10^{-2}$	$(-1.9 + 0.10i) \times 10^{-3}$	$(3.2 - 0.38i) \times 10^{-3}$
q_4	$-0.063 + 0.040i$	$-0.16 + 0.081i$	$(1.5 + 0.054i) \times 10^{-2}$	$(2.3 - 0.059i) \times 10^{-3}$	$(-0.91 + 0.37i) \times 10^{-2}$
q_5	$0.019 - 0.013i$	1.0	$-0.12 + 0.044i$	$(-0.65 + 0.22i) \times 10^{-2}$	$(0.71 + 0.41i) \times 10^{-2}$
q_6	$(-0.62 + 0.49i) \times 10^{-2}$	$-0.13 + 0.042i$	1.0	$(0.74 + 0.46i) \times 10^{-2}$	$-0.11 + 0.022i$
q_7		$(0.91 - 1.2i) \times 10^{-2}$	$-0.091 + 0.019i$	$-0.082 + 0.024i$	1.0
q_8		$(-0.94 + 0.39i) \times 10^{-2}$	$(0.54 - 0.47i) \times 10^{-2}$	1.0	$-0.080 + 0.0098i$
q_9		$(0.15 - 0.23i) \times 10^{-2}$	$(-0.69 + 0.17i) \times 10^{-2}$	$-0.063 + 0.0095i$	$(0.48 - 0.26i) \times 10^{-2}$
q_{10}		$(-0.21 + 0.10i) \times 10^{-2}$	$(1.0 - 0.99i) \times 10^{-3}$	$(0.33 - 0.23i) \times 10^{-2}$	$(-0.65 + 0.96i) \times 10^{-2}$
q_{11}		$(0.43 - 0.74i) \times 10^{-3}$	$(-1.7 + 0.48i) \times 10^{-3}$	$(-0.52 + 0.086i) \times 10^{-2}$	$(0.97 - 0.57i) \times 10^{-3}$
q_{12}		$(-0.68 + 0.41i) \times 10^{-3}$	$(0.35 - 0.34i) \times 10^{-3}$	$(0.76 - 0.51i) \times 10^{-3}$	$(-1.7 + 0.29i) \times 10^{-3}$

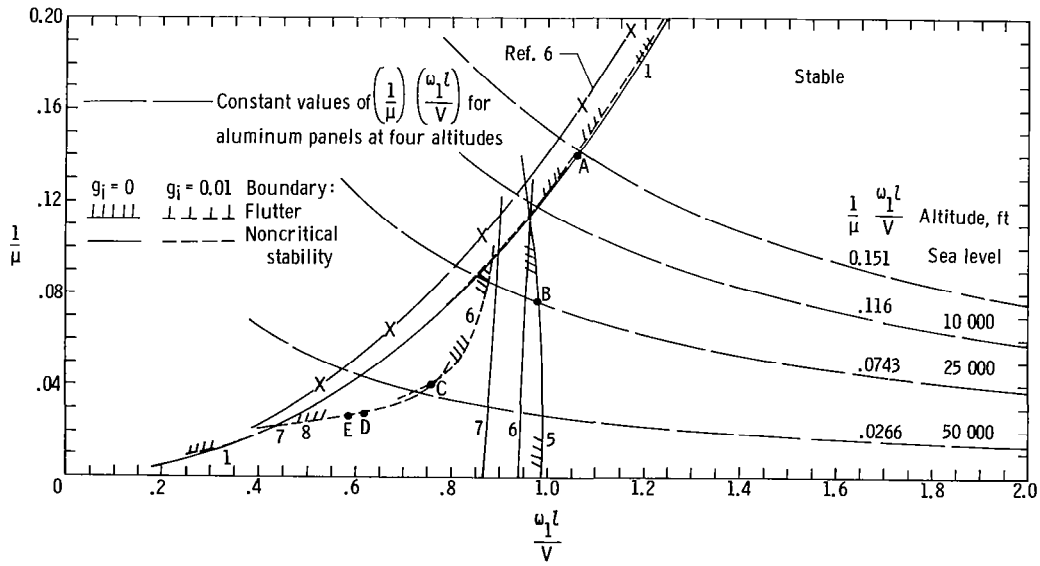

(e) Clamped panel; $\frac{l}{w} = 2$.

Figure 5.- Continued.

Quantity	Point A	Point B	Point C	Point D	Point E
$1/\mu$	0.240	0.1610	0.0861	0.0605	0.0319
g_i	0	0	0.010	0.010	0
k_l	2.33	7.0	8.0	8.0	1.0
$\omega_1 l/V$	2.295	2.020	1.691	1.472	0.9881
ω/ω_1	1.015	3.46	4.72	5.43	1.012
q_1	-0.67 - 0.41i				-0.89 - 0.23i
q_2	1.0				1.0
q_3	-0.61 + 0.32i				-0.48 + 0.085i
q_4	0.20 - 0.21i				0.15 - 0.0035i
q_5	-0.061 + 0.082i	-0.012 + 0.0063i	$(-0.29 + 0.78i) \times 10^{-2}$	$(0.11 - 0.048i) \times 10^{-2}$	-0.047 + 0.011i
q_6	0.020 - 0.032i	0.015 - 0.012i	$(0.31 - 0.17i) \times 10^{-2}$	$(-0.24 + 0.58i) \times 10^{-2}$	0.015 - 0.0038i
q_7	$(-0.63 + 1.3i) \times 10^{-2}$	-0.035 + 0.022i	$(-0.66 + 0.28i) \times 10^{-2}$	$(0.24 - 0.076i) \times 10^{-2}$	$(-0.59 + 0.14i) \times 10^{-2}$
q_8	$(0.18 - 0.59i) \times 10^{-2}$	0.053 - 0.045i	$(0.81 - 0.35i) \times 10^{-2}$	$(-0.52 + 0.21i) \times 10^{-2}$	$(0.21 + 0.066i) \times 10^{-2}$
q_9	$(0.29 + 2.7i) \times 10^{-3}$	-0.28 + 0.16i	-0.019 + 0.0098i	$(0.55 - 0.12i) \times 10^{-2}$	$(-0.85 + 0.30i) \times 10^{-3}$
q_{10}	$(0.20 - 1.5i) \times 10^{-3}$	1.0	0.024 - 0.009i	-0.015 + 0.0085i	$(0.27 - 0.17i) \times 10^{-3}$
q_{11}	$(0.30 + 0.81i) \times 10^{-3}$	-0.25 + 0.10i	-0.17 + 0.090i	0.013 + 0.0017i	$(-0.12 - 0.093i) \times 10^{-3}$
q_{12}	$(-0.30 - 0.53i) \times 10^{-3}$	0.031 - 0.041i	1.0	-0.15 + 0.052i	$(0.17 - 0.65i) \times 10^{-4}$
q_{13}		-0.023 + 0.015i	-0.16 + 0.057i	1.0	
q_{14}		$(0.61 - 0.98i) \times 10^{-2}$	0.013 - 0.016i	-0.10 + 0.034i	
q_{15}		$(-0.64 + 0.48i) \times 10^{-2}$	-0.014 + 0.0064i	$(0.9 - 0.85i) \times 10^{-2}$	
q_{16}		$(0.22 - 0.38i) \times 10^{-2}$	$(0.30 - 0.39i) \times 10^{-2}$	$(-1.1 + 0.38i) \times 10^{-2}$	

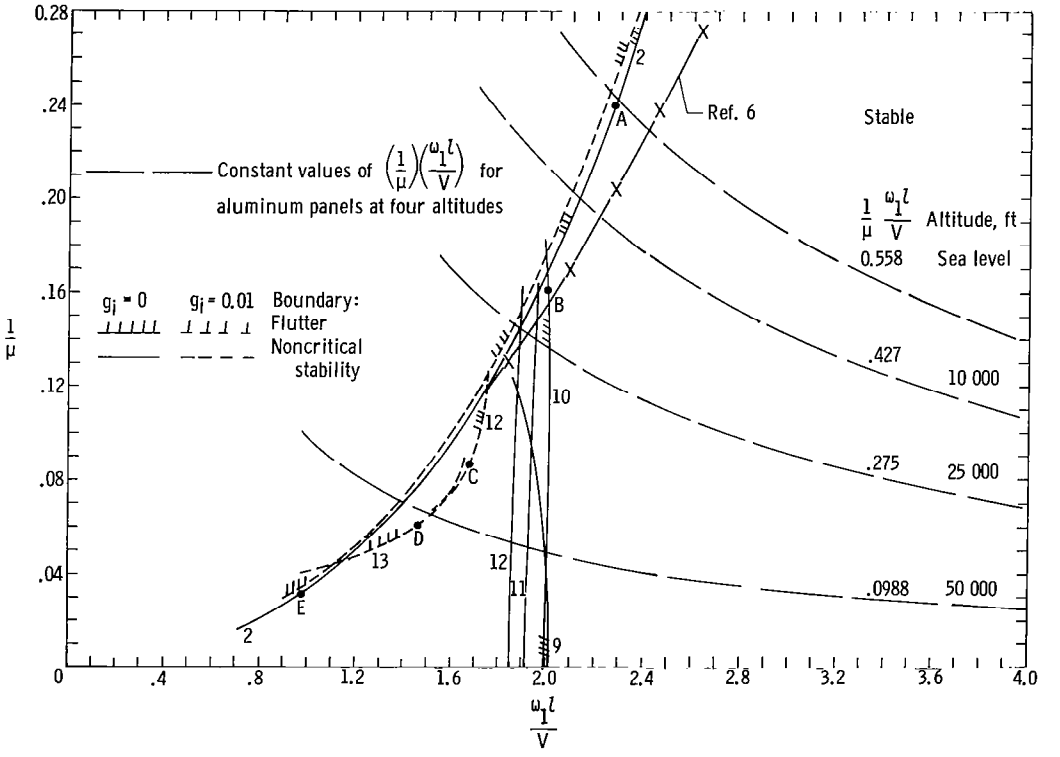

(f) Clamped panel; $\frac{l}{w} = 4$.

Figure 5.- Concluded.

mode-10 boundary. For $g_i = 0.01$, the flutter boundary is formed by portions of the mode-2, mode-12, and mode-13 stability boundaries. For g_i greater than about 0.02, the mode-2 boundary is the flutter boundary in the range of $1/\mu$ shown. For points A and E on the highly coupled boundary, the proportion of natural mode 2 is the largest present as indicated in the table of figure 5(f). An examination of the generalized coordinates (the eigenvectors) indicates that the region of the panel undergoing the greatest amplitude is located well back in the rear half. For each of the points B, C, and D, one mode is predominant in the motion. When these three points were computed, modes 5 to 16 were used in the analysis. The smallness of the coordinates q_5 and q_{16} are considered as an indication that a substantially converged result has been reached. For aluminum panels at sea level, the flutter boundary prescribes $\frac{t}{l} = 0.00180$ for $g_i = 0$ and $\frac{t}{l} = 0.00178$ for $g_i = 0.01$. The parabolic boundary from the closed-form solution falls near the mode-2 boundary and on the conservative side of it.

It should be pointed out that in the section "Results and Discussion" of reference 1, a certain statement lacked a needed qualification. The statement applied to aluminum panels at sea level and was "For all the length-width ratios at least up through 4 on Fig. 3 [of ref. 1], the flutter frequency was near and usually slightly above the first-natural-mode frequency." The statement should have been qualified that for certain of the l/w values, the damping of the panel must be equivalent to a value of g_i of about 0.03 or greater for this generality to be true.

In the section "Analysis" it was stated that the results presented were obtained on the basis of assumed beam modes for both the stream and cross-stream directions. For the panel with all edges clamped, the effects of stiffness cross-coupling between modes are neglected. This cross-coupling occurs because for clamped edges, the integral over the panel of the product of h_i times the second term on the left-hand side of equation (3), $\frac{\partial^4 h_j}{\partial x^2 \partial y^2}$, is nonzero, where the number of half-waves p in the stream direction for mode i plus the corresponding p for mode j is an even number, and the number of half-waves q in the cross-stream direction for mode i plus the corresponding q for mode j is also an even number (in modes i and j, $q = 1$ for the present results). (For sine-wave mode shapes of simply supported panels, the stiffness cross-coupling integral is zero; only the direct term is nonzero where p for mode j equals p for mode i.)

A recent report (ref. 9) gives some quantitative results obtained by including the stiffness coupling terms in a Galerkin modal analysis and using aerodynamic forces from static strip theory. The dynamic-pressure parameter λ increased by 29 percent for $\frac{l}{w} = 4$, and by 12 percent for $\frac{l}{w} = 2$; these increases corresponded to decreases in required panel thickness of about 9 and 4 percent, respectively. Unpublished results obtained at the Langley Research Center agree with the results cited from reference 9, and also show

that with enough modes, the Galerkin solution converges closely to the closed-form result from the Kantorovich method of solving the partial differential equation essentially as in section 8 C of reference 6, except for the minor difference of using the clamped-end-beam fundamental mode for the cross-stream variation instead of the 1.0-minus-cosine variation indicated in equation (8.37) of reference 6.

Thus, for sufficiently high values of l/w, the effects of stiffness cross-coupling become significant and should be taken into account where the more precise results are needed.

Effect of Mach Number

Flutter boundaries have been computed for an aluminum panel at sea level with $\frac{l}{w} = 2$, $g_i = 0$, all edges clamped, and for several Mach numbers in the range from 1.02 to 2.0. The results are given in table III in terms of t/l, $(\beta E/q)^{1/3} t/l$, and $(ME/q)^{1/3} t/l$.

The thickness ratio t/l required to prevent flutter is virtually constant for Mach 1.2 to 1.5, is 5 percent higher at Mach 2.0, 6 percent lower at Mach 1.1, and 16 percent lower at Mach 1.02. This trend for $\frac{l}{w} = 2$ in the low supersonic Mach number range is in sharp contrast to the result for two-dimensional panels $\left(\frac{l}{w} = 0\right)$, for which a great increase in thickness ratio is predicted for Mach numbers less than about $\sqrt{2}$. The ratios of flutter frequency to first natural frequency fell between 1.0 and 1.1 for these solutions for values of g_i near zero. Realizable amounts of structural damping have very little effect on solution values in these cases.

The parameter $(\beta E/q)^{1/3} t/l$ is tabulated as a matter of interest because it is in rather widespread use, having arisen on the basis of the static aerodynamic approximation.

TABLE III.- CLAMPED-EDGE ALUMINUM PANELS WITH $\frac{l}{w} = 2$ AND $g_i = 0$ AT SEA LEVEL

M	t/l	$(\beta E/q)^{1/3} t/l$	$(ME/q)^{1/3} t/l$
1.02	0.00259	0.150	0.258
1.05	.00259	.166	.246
1.1	.00292	.212	.284
1.2	.00311	.241	.294
1.3	.00312	.251	.291
1.4	.00311	.248	.280
1.5	.00311	.247	.272
2.0	.00327	.248	.260

For this panel the parameter is nearly constant for M = 1.2 to 2.0, but drops toward zero in the manner of $\beta^{1/3}$ as M approaches 1.0. The parameter $(ME/q)^{1/3}t/l$ is also tabulated as a matter of interest since some investigators have applied piston-theory aerodynamics to the analysis of panel flutter. It has the feature of remaining finite as M approaches 1.0 for this panel. The values of the two parameters, one with β and the other with M, approach each other as M increases.

CONCLUDING REMARKS

A panel flutter analysis procedure has been developed for which the generalized aerodynamic forces are computed by considering the panel to be finely divided into a large number of boxes and computing the matrix of aerodynamic influence coefficients relating all pairs of boxes. This relatively laborious technique can be resorted to when the aerodynamic forces from simpler expressions are either not obtainable or are of questionable validity. The technique has particular usefulness in applications to finite panels at low supersonic Mach numbers. Flutter solutions are obtained from a modal type of analysis, and all the modal quantities are input information. Either experimental or analytical mode shapes, frequencies, and mass data can be used. Thus, this type of analysis can be applied to any essentially flat panel, whether unstressed or stressed (as by thermal expansion) or whether of isotropic or anisotropic stiffness, and to a small-amplitude flutter superimposed on a buckled deflection.

Results are presented only for flat unstressed isotropic rectangular panels with side edges alined to the airstream direction and with no pressure difference that would tend to bulge the panel. Design-type plots of flutter boundaries are presented for Mach 1.3 for length-width ratios ranging from 0 to 10 for simply supported edges and from 0 to 4 for clamped edges. Additional information is tabulated for a number of points on the flutter boundary of each figure, frequency and flutter-mode-shape information being given to aid in a fuller understanding of the results. For length-width ratios of 1.0 and greater, flutter boundaries obtained from closed-form (nonmodal) solutions based on static strip-theory aerodynamics are included for comparison. A comparison of the dynamic-pressure parameter and of thickness required to prevent flutter shows surprisingly good agreement with the results of the present method for certain ranges of length-width ratio and ratio of air mass to panel mass. These ranges include aluminum panels at sea level, having length-width ratios of 2, 4, and 10 with simply supported edges, and length-width ratios of 2 and 4 with clamped edges.

The effect of Mach number variation for a clamped-edge aluminum panel with a length-width ratio of 2 at sea level was studied. Three different panel flutter parameters are given for Mach numbers in the range from 1.02 to 2.0. With increasing Mach number

over this range, the thickness required to prevent flutter increases somewhat irregularly by about 20 percent.

For clamped-edge panels, the stiffness coupling effects from the assumed beam modes were neglected. A recently published reference reports that inclusion of these coupling effects increased the dynamic-pressure parameter by 12 and 29 percent for length-width ratios of 2 and 4, respectively, as determined on the basis of static strip-theory aerodynamics in a Galerkin analysis using up to 20 beam modes. These and other supporting results indicate that for sufficiently high length-width ratios, the stiffness coupling between beam modes should be taken into account for flutter analysis of clamped-edge panels.

Appendix A gives the form of the expressions used for calculating the mode-shape information used in obtaining the presented flutter boundaries. The form given was adopted because it provides full single-precision accuracy of the mode-shape quantities without the need for multiprecision arithmetic for the higher modes. Appendix B provides conversion formulas for a number of flutter solution parameters in current use. Appendix C describes a way to reduce computing machine time for the large matrix multiplications required to obtain the velocity potentials.

Langley Research Center,
National Aeronautics and Space Administration,
Langley Station, Hampton, Va., June 19, 1966,
126-14-02-01-23.

APPENDIX A

NATURAL MODE CHARACTERISTICS OF RECTANGULAR PANELS

The panel flutter computing program described in the text is designed to accept input information for the downwash, that is, the streamwise slopes and modal deflections obtained from either experiment or analysis. All the panel flutter boundaries given in the present report were obtained with analytically determined downwash input. A description of the derivation of the natural mode shapes employed is given.

For the panel natural vibration modes, it is assumed that separation of the time variable and the two space variables is valid; that is,

$$H_j(x,y,\tau) = \bar{q}_j(\tau)\, h_j(x,y) = q_j e^{i\omega\tau}\, X_j(p,\bar{x})\, Y_j(q,\bar{y}) \tag{A1}$$

where the generalized coordinate q_j can be complex to account for leading or lagging phase relationships in the general flutter motion, and where $X_j(p,\bar{x})$ and $Y_j(q,\bar{y})$ contain the x- and y-variations, respectively, and p and q are the numbers of half-waves of deflection in the x- and y-directions, respectively.

The governing differential equation for small-deflection purely flexural vibrations of a uniform thin isotropic panel with no in-plane loading and unaffected by any surrounding air is

$$D\left[\frac{\partial^4 H_j}{\partial \bar{x}^4} + 2\left(\frac{l}{w}\right)^2 \frac{\partial^4 H_j}{\partial \bar{x}^2 \partial \bar{y}^2} + \left(\frac{l}{w}\right)^4 \frac{\partial^4 H_j}{\partial \bar{y}^4}\right] + m_A l^4 \frac{\partial^2 H_j}{\partial \tau^2} = 0 \tag{A2}$$

As done by several previous investigators (see, for example, refs. 10 and 11), the mode shapes X_j and Y_j of the plate are approximated by the mode shapes for a uniform beam vibrating in flexure. In succeeding sections, certain combinations of edge support are considered. These combinations are (1) all edges simply supported; (2) all edges clamped; (3) leading edge clamped, trailing edge simply supported, and side edges either clamped or simply supported.

Panels Simply Supported at All Edges

The mode shape functions can be given in a form that satisfies both the boundary conditions and the differential equation (A2) and these functions are

$$\left.\begin{aligned} X_j(p,\bar{x}) &= \sin K_p \bar{x} \\ K_p &= p\pi \end{aligned}\right\} \quad (p = 1, 2, 3, \ldots) \tag{A3a}$$

$$\left.\begin{aligned} Y_j(q,\bar{y}) &= \sin K_q\bar{y} \\ K_q &= q\pi \end{aligned}\right\} \quad (q = 1, 2, 3, \ldots) \qquad \text{(A3b)}$$

The natural resonant frequency of mode j as derived by application of Rayleigh's principle of equal maximum kinetic energy and elastic potential energy is

$$\left.\begin{aligned} \omega_j{}^2 &= \frac{D}{m_A l^4}\left(K^*_{p,q}\right)^4 \\ \left(K^*_{p,q}\right)^4 &= K_p{}^4 + 2\left(\frac{l}{w}\right)^2\left(-K_p{}^2\right)\left(-K_q{}^2\right) + \left(\frac{l}{w}\right)^4 K_q{}^4 \end{aligned}\right\} \qquad \text{(A4)}$$

where the combination of indexes p and q is appropriate to mode j.

Panels Clamped on All Edges

For uniform panels the mode shape functions are approximated by uniform-beam mode shapes in both x- and y-directions. More than one form for X_j and Y_j is possible. The following form was adopted because single-precision (nominally, eight-significant-figure) arithmetic operations are sufficient for computing single-precision results for the high modes as well as for the low modes:

$$X_j(p,\bar{x}) = \frac{A_x}{2}\left[\left(1 - \alpha_{p,x}\right)e^{K_p\bar{x}} + \left(1 + \alpha_{p,x}\right)e^{-K_p\bar{x}} + 2\alpha_{p,x}\sin K_p\bar{x} - 2\cos K_p\bar{x}\right] \qquad \text{(A5a)}$$

$$Y_j(q,\bar{y}) = \frac{A_y}{2}\left[\left(1 - \alpha_{q,y}\right)e^{K_q\bar{y}} + \left(1 + \alpha_{q,y}\right)e^{-K_q\bar{y}} + 2\alpha_{q,y}\sin K_q\bar{y} - 2\cos K_q\bar{y}\right] \qquad \text{(A5b)}$$

where the amplitude factors A_x and A_y are chosen as unity so that

$$\left.\begin{aligned} \int_0^1 X_j{}^2 d\bar{x} &= A_x{}^2 = 1 \\ \int_0^1 Y_j{}^2 d\bar{y} &= A_y{}^2 = 1 \end{aligned}\right\} \qquad \text{(A6)}$$

The characteristic values K_p and K_q are the roots of the characteristic equations

$$\cos K_p \cosh K_p = 1 \qquad \text{(A7a)}$$

$$\cos K_q \cosh K_q = 1 \qquad \text{(A7b)}$$

from which it is found that

$$K_p = \left(p + \frac{1}{2}\right)\pi - \epsilon_p \qquad \left(|\epsilon_p| << 1.0\right) \qquad \text{(A8a)}$$

$$K_q = \left(q + \frac{1}{2}\right)\pi - \epsilon_q \qquad \left(|\epsilon_q| << 1.0\right) \qquad \text{(A8b)}$$

The small quantities ϵ_p and ϵ_q rapidly become even smaller as p and q increase, and the labor of determining them is eased by using their asymptotic values for the higher values of p and q:

$$\epsilon_p \sim 2(-1)^p e^{-\left(p+\frac{1}{2}\right)\pi} \qquad \text{(A9a)}$$

$$\epsilon_q \sim 2(-1)^q e^{-\left(q+\frac{1}{2}\right)\pi} \qquad \text{(A9b)}$$

The quantities $\alpha_{p,x}$ and $\alpha_{q,y}$ are

$$\alpha_{p,x} = \frac{\cosh K_p - \cos K_p}{\sinh K_p - \sin K_p} \qquad \text{(A10a)}$$

$$\alpha_{q,y} = \frac{\cosh K_q - \cos K_q}{\sinh K_q - \sin K_q} \qquad \text{(A10b)}$$

For the evaluation of X_j and Y_j from equations (A5a) and (A5b), the values of $1 - \alpha_{p,x}$ and $1 - \alpha_{q,y}$ to single-precision accuracy are required; for this evaluation their asymptotic values for high p and q are helpful

$$1 - \alpha_{p,x} \sim -\epsilon_p \qquad \text{(A11a)}$$

$$1 - \alpha_{q,y} \sim -\epsilon_q \qquad \text{(A11b)}$$

Values of K_p, K_q, $1 - \alpha_{p,x}$, and $1 - \alpha_{q,y}$ for values of p and q ranging from 1 to 18 and for opposite-edge pairs clamped are given in the following table:

APPENDIX A

p or q	K_p or K_q	$1.0 - \alpha_{p,x}$ or $1.0 - \alpha_{q,y}$
1	4.7300407	$0.17497779 \times 10^{-1}$
2	7.8532045	$-.77722999 \times 10^{-3}$
3	10.995608	$.33551562 \times 10^{-4}$
4	14.137165	$-.14498945 \times 10^{-5}$
5	17.278760	$.62655621 \times 10^{-7}$
6	20.420352	$-.27075949 \times 10^{-8}$
7	23.561945	$.11700579 \times 10^{-9}$
8	26.703538	$-.50562789 \times 10^{-11}$
9	29.845130	$.21850161 \times 10^{-12}$
10	32.986723	$-.94423106 \times 10^{-14}$
11	36.128316	$.40803924 \times 10^{-15}$
12	39.269908	$-.17632974 \times 10^{-16}$
13	42.411501	$.76198991 \times 10^{-18}$
14	45.553093	$-.32928570 \times 10^{-19}$
15	48.694686	$.14229725 \times 10^{-20}$
16	51.836279	$-.61492218 \times 10^{-22}$
17	54.977871	$.26573197 \times 10^{-23}$
18	58.119464	$-.11483320 \times 10^{-24}$

For an isotropic material, application of the Rayleigh principle leads to the expression for the natural frequency of mode j of a plate

$$\left.\begin{aligned} \omega_j^2 &= \frac{D}{m_A \ell^4}\left(K^*_{p,q}\right)^4 \\ \left(K^*_{p,q}\right)^4 &= K_p^4 + \left(\frac{\ell}{w}\right)^4 K_q^4 + 2\left(\frac{\ell}{w}\right)^2 \alpha_{p,x} K_p \left(2 - K_p \alpha_{p,x}\right) \alpha_{q,y} K_q \left(2 - K_q \alpha_{q,y}\right) \end{aligned}\right\} \qquad \text{(A12)}$$

where the stiffness coupling effects are neglected. The combination of p and q is that appropriate to mode j.

As was pointed out at the beginning of this section, equations (A5a) and (A5b) give approximations for the plate mode shape. The boundary conditions are satisfied but the differential equation (A2) is satisfied only approximately. The differential equation for a plate could be satisfied with greater accuracy by using a series of terms of the beam-mode type. What is done here, as has been done by many investigators, is to use only the one predominant term in a series for each mode j and to neglect the other terms on the grounds that their effect is minor, not of the first order. Recently published findings

of reference 9 regarding the effects on some flutter solutions of including the stiffness coupling terms are described for clamped-edge panels in the section "Results and Discussion."

Panels Clamped at Leading Edge and Simply Supported at Trailing Edge

For a panel clamped at its leading edge and simply supported at its trailing edge, the function X_j is again approximated by that for a beam with the same boundary conditions. Thus, X_j has the same form as in equation (A5a) but the characteristic values of K_p are obtained from the characteristic equation

$$\tan K_p = \tanh K_p \tag{A13}$$

the roots of which are

$$K_p = \left(p + \frac{1}{4}\right)\pi - \epsilon_p \qquad \left(|\epsilon_p| \ll 1\right) \tag{A14}$$

and for the higher values of p the asymptotes are

$$\epsilon_p \sim e^{-2\left(p+\frac{1}{4}\right)\pi} \tag{A15}$$

$$1 - \alpha_{p,x} \sim -2\epsilon_p \tag{A16}$$

The quantities K_p and $1 - \alpha_{p,x}$ are given in the following table for leading edge clamped, trailing edge simply supported, and for values of p from 1 to 6:

p	K_p	$1.0 - \alpha_{p,x}$
1	3.9266023	$-0.77731188 \times 10^{-3}$
2	7.0685827	$-.14498977 \times 10^{-5}$
3	10.210176	$-.27075950 \times 10^{-8}$
4	13.351769	$-.50562785 \times 10^{-11}$
5	16.493361	$-.94423105 \times 10^{-14}$
6	19.634954	$-.17632974 \times 10^{-16}$

If the amplitude factor A_x is chosen as unity,

$$\int_0^1 X_j^2 d\bar{x} = A_x^2 = 1$$

The natural frequency of the panels depends on the type of support at the side edges.

APPENDIX A

Simply supported side edges.- For simply supported side edges Y_j and K_q are given by equation (A3b). There is no stiffness coupling and the natural frequencies are given by

$$\left.\begin{aligned} \omega_j^2 &= \frac{D}{m_A \ell^4}\left(K^*_{p,q}\right)^4 \\ \left(K^*_{p,q}\right)^4 &= K_p^4 + \left(\frac{\ell}{w}\right)^4 K_q^4 + 2\left(\frac{\ell}{w}\right)^2 \alpha_{p,x} K_p \left(1 - K_p \alpha_{p,x}\right)\left(-K_q^2\right) \end{aligned}\right\} \tag{A17}$$

Clamped side edges.- For clamped side edges Y_j is given by equation (A5b); K_q, by equation (A7b); and $\alpha_{q,y}$, by equation (A10b). (The latter two quantities are obtained from the table following equation (A11).) When stiffness coupling is neglected, the natural frequencies are given by

$$\left.\begin{aligned} \omega_j^2 &= \frac{D}{m_A \ell^4}\left(K^*_{p,q}\right)^4 \\ \left(K^*_{p,q}\right)^4 &= K_p^4 + \left(\frac{\ell}{w}\right)^4 K_q^4 + 2\left(\frac{\ell}{w}\right)^2 \alpha_{p,x} K_p \left(1 - K_p \alpha_{p,x}\right)\alpha_{q,y} K_q \left(2 - K_q \alpha_{q,y}\right) \end{aligned}\right\} \tag{A18}$$

Panels With Various Edge Supports, Orthotropicity, and In-Plane Loadings

A recent significant contribution to the analysis of vibration of rectangular panels is made by reference 12 which treats a variety of edge restraints including simply supported, clamped, and elastic restraint against rotation. Account is taken of in-plane compressive and tensile loads in both directions and of orthotropic stiffness of the panel. Analysis is made by the method of Kantorovich, which involves an assumption of the modal deflection shape in one direction, a consequent reduction of the partial differential equation in two independent space variables to an ordinary differential equation in a single independent space variable, and its eigensolution. Solutions that satisfy the plate differential equation exactly are obtained if the assumed deflection mode in one direction is between simply supported edges. Extensive tables are provided in reference 12 for the use of the analyst.

APPENDIX B

RELATIONS AMONG SOME PANEL FLUTTER PARAMETERS IN THE LITERATURE

The flutter boundaries of the present report are presented in terms of a mass ratio $1/\mu$ plotted against a stiffness parameter $\omega_1 l/V$. Their relation to some other parameters in the panel flutter literature is explained briefly here, specifically for isotropic panels only.

A parameter having rather wide use (in refs. 4 and 5, for example) in a variety of forms is a panel flutter dynamic-pressure parameter defined by

$$\lambda \equiv \frac{\rho V^2 l^3}{\beta D} = \frac{2ql^3}{\beta D} = \frac{24q(1 - \nu^2)}{\beta E}\left(\frac{l}{t}\right)^3 \tag{B1}$$

where q is stream dynamic pressure, and E is Young's modulus of elasticity. The relationship of λ to the parameters of the present report is

$$\lambda = \left(K^*_{1,1}\right)^4 \frac{1}{\beta} \frac{1/\mu}{\left(\omega_1 l/V\right)^2} \tag{B2}$$

and $\left(K^*_{1,1}\right)^4$ is given in appendix A for several edge-support conditions. (Assign $p,q = 1,1$.) The dynamic-pressure parameter is seen in a variety of forms; some of these replace β by M, drop β entirely, drop the factor 24, drop the quantity $(1 - \nu^2)$, introduce the factor π^4, and so forth. Other variations are the cube root and the inverse cube root $\lambda^{1/3}$. The inverse cube root has the merit that the thickness to prevent flutter, and thus the weight penalty, are contained linearly. The relationships among such variations of λ are readily apparent.

In reference 13 the flutter boundaries are on plots for which the relation of the coordinates to λ and to the present parameters may not be as clear. The vertical coordinate is $\tau\left[\frac{E}{\rho c_\infty^2(1 - \nu^2)}\right]^{1/3}$ which is equal to $\left(\frac{24M^2}{\beta\lambda}\right)^{1/3}$. The horizontal coordinate is $\frac{c_\infty \rho_s}{\rho}\left[\frac{\rho_s(1 - \nu^2)}{E}\right]^{1/2}$ which equals $\left(\frac{1}{\mu}\frac{\omega_1 l}{V}\right)^{-1}\frac{\left(K^*_{1,1}\right)^2}{M\sqrt{12}}$. The symbols from reference 13, τ, c_∞, and ρ_s are t/l, a_s, and m_A/τ, respectively, in the present report.

APPENDIX C

MATRIX OPERATIONS FOR COMPUTING THE VELOCITY POTENTIAL MATRIX OF EQUATION (27)

The practicality of this box method is largely dependent upon the cost of the computing machine time required. This time is significantly influenced by equation (27). Not only should the multiplication be carried out completely within the machine core, but also the matrices should occupy as small a portion of the core as possible, consistent with the desirably low machine time for the overall program. Thus, any repetition of the storage of a given number should be avoided.

If the $\{A_\varphi(r,s)\}$ were indeed a single-column matrix, the rectangular matrix of complex downwash ratios would have $B_S B_{XS}$ rows and nearly $2B_S B_{XS}$ columns, nearly half of the elements would be zero, and all the nonzero elements would be repeated from at least B_{XS} to as much as $B_S B_{XS}$ times. But by an arrangement of the submatrices that can be described as "folded," repetition of the submatrices of the downwash is avoided.

As an illustration, for the simple case of $B_S = 5$ and $B_{XS} = 3$, let the elements of the downwash matrix $\left[\frac{\partial h_j}{\partial \bar{x}} + i\,\frac{\omega l}{V}\,h_j\right]$ be represented by their indexes μ,ν, and let zero elements be indicated by a blank. Then that "folded" matrix is as follows:

$$\left[\begin{array}{ccccc|ccccc|ccccc}
4,2 & 3,2 & 2,2 & 1,2 & 0,2 & 4,1 & 3,1 & 2,1 & 1,1 & 0,1 & 4,0 & 3,0 & 2,0 & 1,0 & 0,0 \\
3,2 & 2,2 & 1,2 & 0,2 & & 3,1 & 2,1 & 1,1 & 0,1 & & 3,0 & 2,0 & 1,0 & 0,0 & \\
2,2 & 1,2 & 0,2 & & & 2,1 & 1,1 & 0,1 & & & 2,0 & 1,0 & 0,0 & & \\
1,2 & 0,2 & & & & 1,1 & 0,1 & & & & 1,0 & 0,0 & & & \\
0,2 & & & & & 0,1 & & & & & 0,0 & & & &
\end{array}\right] \qquad \text{(C1)}$$

If the elements of the matrix $A_\varphi(r,s)$ are represented by their indexes r,s that matrix is, in effect

APPENDIX C

$$\left[\begin{array}{ccc}
0,0 & 0,1 & 0,2 \\
1,0 & 1,1 & 1,2 \\
2,0 & 2,1 & 2,2 \\
3,0 & 3,1 & 3,2 \\
4,0 & 4,1 & 4,2 \\
\hline
0,1 & 0,0 & 0,1 \\
1,1 & 1,0 & 1,1 \\
2,1 & 2,0 & 2,1 \\
3,1 & 3,0 & 3,1 \\
4,1 & 4,0 & 4,1 \\
\hline
0,2 & 0,1 & 0,0 \\
1,2 & 1,1 & 1,0 \\
2,2 & 2,1 & 2,0 \\
3,2 & 3,1 & 3,0 \\
4,2 & 4,1 & 4,0
\end{array}\right] \qquad \text{(C2)}$$

The resulting folded $\left[\varphi_j{}^*(m,n)\right]$ matrix of equation (27), represented by its indexes m,n is then

$$\left[\begin{array}{ccc}
4,2 & 4,1 & 4,0 \\
3,2 & 3,1 & 3,0 \\
2,2 & 2,1 & 2,0 \\
1,2 & 1,1 & 1,0 \\
0,2 & 0,1 & 0,0
\end{array}\right] \qquad \text{(C3)}$$

In practice an actual arrangement of the $A_\varphi(r,s)$ matrix elements as shown in matrix (C2) with repetition of elements (due to right-left symmetry) would be prohibitively wasteful of memory-storage space. It is a simple matter to arrange the elements in a single one-dimensional column array and select appropriate subcolumns as needed. With a little more ingenuity the necessary subcolumns can be used without any storage duplication of elements such as that shown in the middle column of the $A_\varphi(r,s)$ matrix (C2). For the same reason, for the $\left[\frac{\partial h_j}{\partial \bar{x}} + i\,\frac{\omega l}{V}\,h_j\right]$ matrix (C1) the storage space need be no larger than the top row (B_s times B_{xs} complex numbers). Successive rows can be formed in the same space by shifting elements and inserting zeros. Thus, the $\left[\varphi_j{}^*(m,n)\right]$ matrix (C3) is obtainable in a systematic and economic manner for each mode.

For subsequent use in equation (29) the $\left\{\varphi_j{}^*(m,n)\right\}$ matrix must be "unfolded" into a single column, the subcolumns of which are the columns of the folded matrix (C3).

REFERENCES

1. Cunningham, H. J.: Flutter Analysis of Flat Rectangular Panels Based on Three-Dimensional Supersonic Potential Flow. AIAA J., vol. 1, no. 8, Aug. 1963, pp. 1795-1801.

2. Watkins, Charles E.: Three Dimensional Supersonic Theory. Aerodynamic Derivatives, Pt. 2 of AGARD Manual on Aeroelasticity, ch. 5, W. Prichard Jones, ed.

3. Milne, William Edmund: Numerical Calculus. Princeton Univ. Press, 1949.

4. Bohon, Herman L.; and Dixon, Sidney C.: Some Recent Developments in Flutter of Flat Panels. J. Aircraft, vol. 1, no. 5, Sept.-Oct. 1964, pp. 280-288.

5. Hedgepeth, John M.: Flutter of Rectangular Simply Supported Panels at High Supersonic Speeds. J. Aeron. Sci., vol. 24, no. 8, Aug. 1957, pp. 563-573, 586.

6. Houbolt, John C.: A Study of Several Aerothermoelastic Problems of Aircraft Structures in High Speed Flight. Nr. 5, Mitt. Inst. Flugzeugstatik Leichtbau, Leeman (Zurich), c.1958.

7. Nelson, Herbert C.; and Cunningham, Herbert J.: Theoretical Investigation of Flutter of Two-Dimensional Flat Panels With One Surface Exposed to Supersonic Potential Flow. NACA Rept. 1280, 1956. (Supersedes NACA TN 3465.)

8. Anon.: U.S. Standard Atmosphere, 1962. NASA, U.S. Air Force, and U.S. Weather Bur., Dec. 1962.

9. Dowell, E. H.: Experimental and Theoretical Panel Flutter Studies in the Mach Number Range of 1.0 to 5.0. ASD-TDR-63-449, Suppl. 1, U.S. Air Force, Aug. 1965. (Available from DDC as AD622831.)

10. Young, Dana: Vibration of Rectangular Plates by the Ritz Method. J. Appl. Mech., vol. 17, no. 4, Dec. 1950, pp. 448-453.

11. Warburton, G. B.: The Vibration of Rectangular Plates. Proc. Inst. Mech. Eng. (London), vol. 168, no. 12, 1953, pp. 371-384.

12. Weeks, George E.; and Shideler, John L.: Effect of Edge Loadings on the Vibration of Rectangular Plates With Various Boundary Conditions. NASA TN D-2815, 1965.

13. Kobett, D. R.; and Zeydel, E. F. E.: Research on Panel Flutter. NASA TN D-2227, 1963.